Universitá degli studi di Parma
Dottorato di ricerca in scienza e tecnologie dei materiali innovativi

XXVI Ciclo

The Hydrogen Storage in Alkali-Transition metal Fullerides

Matteo Aramini

Coordinatore:
Chiarissimo Prof. Enrico Dalcanale
Relatore:
Chiarissimo Prof. Mauro Riccò

A thesis submitted for the degree of Philosophiæ Doctor
in Innovative Materials Science and Technology

To the people that inspired, supported and protected me & to those who
were willing to scratch beneath the surface to know me...

ǿ δϵ̀ άνϵξϵ́ταστøζ βίøζ øύ βιωτø̀ζ άνθρώπω

The unexamined life is not worth living
Plato - *Apology*

Contents

Abstract

Intercalated alkali metal fullerides, which have been recently demonstrated promising hydrogen storage materials, have been prepared and characterized by μSR spectroscopy, known technique for the study of the interaction of the hydrogen atom with matter. The hydrogenation mechanism has been clarified and highligted the possible improvement with the addition of transition metal particles. Novel synthetic strategies have been developed to achieve the addition of platinum, palladium and nickel to lithium intercalated fullerides and the new materials were characterized with multiple solid state techniques aiming to probe their structures and understand the remarkable absorption properties which were discovered by manometric and calorimetric techniques.

1

Introduction

1.1 Energy problems & Hydrogen-based Solutions

Massive use of fossil fuels as an energy source led environmental consequences such as an anthropogenic increase in the amount of nitrogen/carbon-based gases in the atmosphere and a corresponding rise in the global average near surface temperature known as greenhouse effect. Moreover to withstand global energy demand, which is forecast to double by 2050 (United States Department of Energy, US-DoE), it is necessary to establish a transition from the non-renewable oil/gas dependance to a renewable energies based economy. In this context hydrogen may replace fossil fuels and natural gases: its chemical energy (142 MJ kg^{-1}) is three times bigger than liquid hydrocarbons and its combustion processes in fuel cells represent a carbon-free method of heat and electricity generation compatible with many domestic and industrial applications. The oxydation reaction with oxygen leads to the formation of water or steam that is naturally part of the water cycle. The main technical problem the hydrogen economy is facing is provided by H_2 storage media. Classical high pressure tanks exploit gas phase storage but in order to realise a petrol equivalent tank around 450 litres space would be necessary under 300 bar compression which constitutes a dangerous system. The liquid hydrogen density (70.8 kg m^{-3}) could help optimising space problems but the hydrogen condensation temperature is 21 K and therefore cryotechniques, which are inherently unsafe, would be needed. Luckily often hydrogen is absorbed in solid state materials with a density even higher than gas and liquid state (1). Metal hydrides as i.e. $LaNi_5H_6$ and Mg_2NiH_4 have a high volumetric hydrogen density between 90 and

150 kgH_2 m^3, but the high density of the host material limits the achievement of low gravimetric hydrogen density between 1 and 5 wt% (2). On the other hand different chemical hydrides, as for example the reaction of $NaBH_4$ with H_2O to form $NaBO_4$ and 4 H_2, have a high gravimetric hydrogen density of 10.8 wt% but the product is too stable and is energetically too expensive to reverse the reaction (3). In mobile application, carbon based systems are inherently safer than many others systems due to the chemical inertness of carbon compared to the high reactivity of borohydrides, alanates with air and water. Moreover carbon based materials are to be considered relatively unexpensive with respect to transition metal and rare-earth based compounds, thus more suitable for widespread application.

1.2 De Fullerenis Molecula

Named after the American architect Buckminster Fuller, the carbon allotrope and most abundant fulleroid C_{60} has opened an entire research field in carbon chemistry and physics after its discovery in 1985 (4) and the adoption of Krätschmer and Huffman large scale production method (5). This molecule is composed by 60 carbon atoms which are arranged in 12 pentagons and 20 hexagons rings (see Fig. 1.1: in comparison with the purely sp^2 plane of graphite it is possible to understand that 5 member rings force the plane into a curved configuration. According to Eulers theorem 12 pentagons lead to the smallest closed structure achievable. The truncated icosahedrons (point group Ih) resulting geometry has a surface radius of about 3.56 $\dot{A}$, but the outer diameter is increased to 10 $\dot{A}$ for the surface occupation of molecular orbitals around the carbon shell. Moreover the p electrons are not homogeneously delocalised on the sphere and provide two different bonds: the edge shared by two hexagons is 1.46 $\dot{A}$, the one between an hexagon and a pentagon is 1.40 $\dot{A}$.

As shown in Fig. 1.1 fullerenes arrange into a face centered cubic structure (space group F m$\bar{3}$m) with a=14.17 $\dot{A}$ at 300 K and inter-fullerene distance of 10.02 $\dot{A}$. Above 260 K molecules are free to rotate around their mass center in a merohedral disordered plastic crystal. A temperature decrease freezes the rotation changing structure into a simple cubic cell (space group Pa3) (6). The high molecular simmetry provides two different energy scales: one is associated with the strong intramolecular covalent bonds and a weaker one due to Van der Waals soft interball binding. This feature deeply

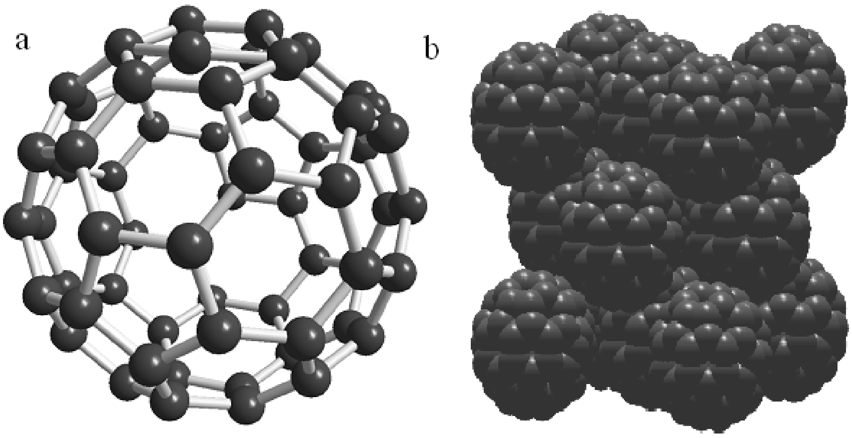

Figure 1.1: a: a schematic representation of the fullerene molecule; b: the crystal *fcc* structure of solid C_{60}.

influences the electronic behavior: the solid states resembles the molecular levels with the addition of a weak splitting in narrow bands (see Fig. 1.2).

The lowest unoccupied molecular orbital (LUMO) presents a non bonding nature in agreement with the C_{60} electronegative character and is triply degenerate (t_u simmetry). Electrochemical measurements on fullerene solutions (7, 8) explored the progressive filling of these orbitals and showed the presence of C_{60}^{n-} states (n up to 6). Moreover, intercalation of alkali metal ions indicated the possibility of reaching anion charges of 12^- (9) (allowing the population of t_{1g} LUMO level)

1.3 Intercalated Fullerides

The fullerene low reduction potential and its internal available free volume in the crystal lattice provided intercalation chemistry a fertile soil for the insertion of an incredibly wide number of electron donors. This resulted in the study of many charge transfer salts called fullerides, whose main properties come from the partial or complete filling of the electronic band structure. The undoped C_{60} is a semiconductor whose band gap is around 1.7 eV. During electron addition, the conduction band is progressively filled and transport properties are changed. Intercalation of alkali atoms in a stoichiometry A_xC_{60} yields a complex behaviour in these systems. K_3C_{60} reports a metallic phase with a superconducting transition (T_C =19 K) due to the half filling of its t_{1u} orbital (10, 11),

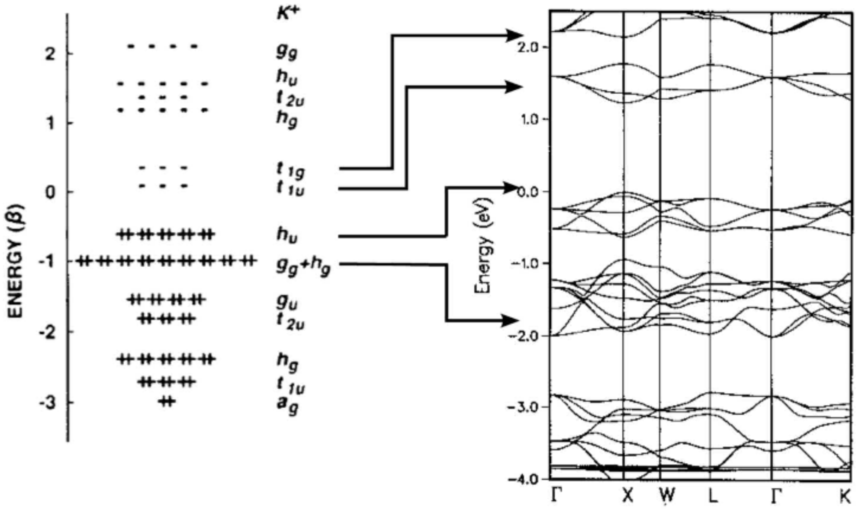

Figure 1.2: C_{60} molecular orbitals and electronic band structure of the molecular crystal.

while K_6C_{60} is an insulator. Probably due to strong electron correlation (12) deviations are commonly observed: i.e. K_4C_{60} shows insulating ground state (13, 14). Stimulated by the studies on fulleride superconductivity, the scientific community developed a huge amount of intercalation compounds (15). Most of alkali and alkali-earth metal ions were added to C_{60} in order to explore tunable fulleride properties (the identification of a proper bibliography would be an immense task and therefore only some publication on different ionic systems are mentioned here: (16, 17, 18, 19, 20)). This investigation was as well extended to halogen atoms (21) and to some rare earth metals (22, 23, 24). Nowadays it is easily possible to synthetise a huge number of intercalated fullerides.

1.4 Why H_2 Storage in Carbon Nanostructures?

Carbon materials are nowadays considered a promising system for hydrogen storage alternative to the common metal hydride and metal organic framework. Their relatively light weight suggests a possible use in the vehicle application and their relatively unexpensive costs may promote a widespread distribution.

Besides the aforementioned advantages, pure carbon systems like graphite, even if nanostructured, still reveal inadequate for this purpose. The binding energy of hydrogen molecules to carbon framework represents the main problem to be solved. H_2 can either be physisorbed on carbon (as it is currently observed at very low temperatures) but this process involves a low binding energy (5 kJ mol^{-1}) which is too small for storage application (25) or, on the other hand, the hydrogen molecule can be chemisorbed after dissociation by the formation of a direct C-H bond on top of carbon sp^2 layers. In this case, the binding energy is around 140 kJ/mol, still far beyond the targeted value of 15-20 kJ mol^{-1} which represents the optimal value for near room temperature reversible applications.

Such an energy range may be achieved by promoting binding mechanisms which are different from the bare and too weak physisorption or from the too strong chemisorption. As a general consequence of partial sp^2-sp^3 hybridization the hydrogen binding energy has been calculated to increase with increasing curvature (26), These structure can be naturally realised by folding carbon planes either in cylindrical (to form nanotubes) or spherical way by introducing pentagon rings in the hexagonal lattice (to form fullerenes). Early results on carbon nanotubes gave absorptions in the range of 5-10 wt% at 77 K (25) although precise numbers are hardly obtained due to difficulties in sample purification from metal catalysts. On the other hand, carbon nanohorns show a binding energy in the range 10-12 kJ mol^{-1} (27) and an adsorbate density higher than that of the liquid H_2 at 20 K is predicted (28). Even graphite highlights remarkable uptake properties leading to a few percent physisorption at 77 K (1) but its energy range exclude any room temperature stability. If the hydrogen is chemisorbed the result is an sp^3 carbon structure which traps around 7 wt% but in a too stable chemisorption driven graphane (29).

A further increase in binding energy can be reached if the curved sheet is charged. Both nanotubes and fullerenes clearly show this feature. Although the early reports on alkali doped nanotubes (30) largely exceed the US-DoE target of 6.5 wt% they were not subsequently confirmed (31) and attributed to the presence of metal catalyst. However lithium intercalated CNT (32) show evidences about a clear increase in H_2 uptake with respect to the neutral material. Similarly DFT calculations show that the binding strength of molecular hydrogen on either positively or negatively charged fullerenes can be dramatically enhanced to 18-22 kJ mol^{-1} (33). In both cases the enhancement is attributed to the polarization of the hydrogen molecule by the electric field generated near the surface of the charged nanostructure.

Therefore a great importance for the tayloring of hydrogen storage materials is held by the establishment of a strong interaction between H_2 and metal ions. Two possible sources motivate this binding: the first is the electrostatic interaction since the leading permanent multiple moment of H_2 is its small quadrupole moment which can couple to other charges. From the value of $2.21 \cdot 10^{-40}$ Cm^2, an approximate interaction of 3.5 kJ mol^{-1} with a point charge at 3 $\dot{A}$ distance can be estimated. Furthermore the hydrogen molecule is moderately polarizable ($\chi_{H2} = 8.79 \cdot 10^{-41}$ $C^2m^2J^{-1}$). This adds to the previously estimated energy approximatively 6.8 kJ mol^{-1} and is the dominant one in the case of alkali metal ions. The second interaction is the orbital one. Unlike the overall repulsive behaviour of two filled orbitals, the interaction of a filled one with the empty one belonging to different systems can be attractive due to partial charge transfer and donor-acceptor bonding interaction. This can be much stronger than the former and adds to the electrostatic one when H_2 gets close to alkaline earth ions or transition metal ions. If we focus our attention on the most lightweight alkali or alkaline-earth elements it is known (34) that the bond between Li^+ and molecular hydrogen is strong enough to fall into the useful range of ideal binding affinities. This interaction is predominantly of electrostatic charge-quadrupole and charge-induced dipole character. But if the presence of C_{60} as electron acceptor is included into the ab-initio calculation, Na^+ turns out to be favourite as a H_2 absorber (35). Instead a different situation is met for Mg^{2+} and Al^{3+} where their low lying vacant valence orbitals of favourable symmetry can mix with the bonding hydrogen orbital allowing a forward donation of the H_2 σ electron density into the vacant orbital (34) followed by a back donation from the metal to the anti-bonding σ^* H_2 orbital. As a result the H-H bond is lengthened considerably and the metal-hydrogen bond gets stabilized. The obtained binding energy is rather strong and actually often overcomes the 20-40 kJ mol^{-1} useful range. This interaction is effective also in transition metals where it produces comparable (or higher) binding energies and it is known as Kubas interaction (36), which can be exploited in the design of hydrogen storage materials (37).

Usually bare metal ions bind hydrogen too strongly for an ideal and reversible gas storage. However this picture can dramatically change when metals are complexed and only part of their electron density is available to interact with H_2 orbitals. In this case the binding energy can be suitably reduced to fit the useful range, as predicted on metal-ethylene complexes which should efficiently store hydrogen exceeding 14 wt% (38, 39).

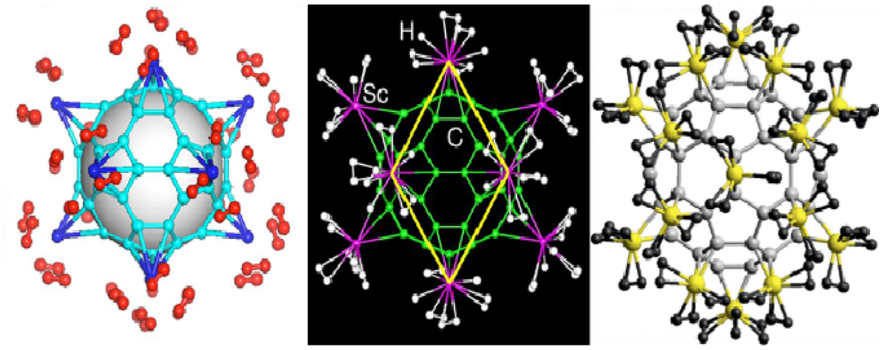

Figure 1.3: Computed structures of $Ti_{12}C_{60}$, $Sc_{12}C_{60}$ and $Ni_{30}C_{60}$ (from the left). The H_2 molecules they can adsorb are also represented.

Carbon nanostructures and, mainly, fullerenes proved to be the ideal framework for metal complexation since: a) the Dewar coordination (40, 41, 42) between ions and the cyclopentadiene rings facilitates every metal bonding; b) the relatively weak strength of this bond allows the metal activity in the development of further bonds with large amounts of H_2 molecules; c) the high surface area and large empty volume in the fullerene lattice allows a fast and efficient H_2 intersticial diffusion thus enhancing the sorption/desorption dynamics. As a matter of fact, several first principle calculations recently reported clearly show either the stability of different metal decorated C_{60} and their high H_2 uptake at the useful energy range. Ti is predicted to decorate C_{60} with stoichiometry ranging from 12 to 14 yielding up to 7.5 wt% H_2 at an energy of 50 kJ mol^{-1} (43); $Sc_{12}C_{60}$ is predicted to bind 7 wt% of hydrogen at 30-40 kJ mol^{-1} (44); Ni is foreseen to bind to the 6-6 bonds of C_{60} thus allowing 30 Ni atoms to attach to fullerene, yielding an uptake of 6.8 wt% at an energy of 50 kJ mol^{-1} (45) (see computational structures in Fig. 1.3).

Similar clusters with comparable absorption uptake and binding energies were also computed for alkali and alkali-earth metals. In particular $Li_{12}C_{60}$ was predicted to have a record storage capacity of 13 wt% with 18 kJ mol^{-1} binding energy (46). Similarly, Ca was shown to develop a coating of the C_{60} molecule (47) (see Fig. 1.4) by coordinating to both pentagons and hexagons thus giving a fulleroid whose stoichiometry is $Ca_{32}C_{60}$ and which has capability of 8.4 wt% H_2 storage with 20-40 kJ mol^{-1} binding energy.

Similar features are expected also for Sr (47). Every compound presented so far reflects the enhancement of the physical absorption of hydrogen molecules in terms of

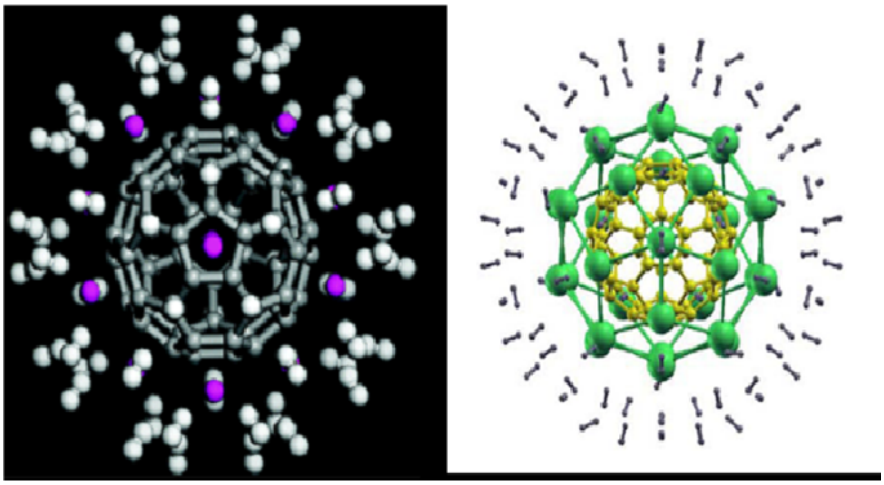

Figure 1.4: Computed structures of $Li_{12}C_{60}$ and $Ca_{32}C_{60}$ (from the left) and their estimated adsorbed H_2.

binding energy. The intercalation of metal atoms in fullerides is expected to lower the chemical absorpion energy promoting an heterogeneous catalysis of hydrogen dissociation on supported metal catalysts, described as spillover effect (48). Hydrogen spillover is dissociative chemisorption of H_2 onto a metal particle followed by migration of hydrogen atoms onto the surface of the bulk material and subsequent diffusion away from the receptor site (49, 50) It was recently proposed that an enhancement of the hydrogen storage capacities of physisorptive materials can be gained by hydrogen spillover from a metal catalyst onto the adsorbing surface (51, 52, 53, 54). The details of hydrogen spillover are not yet understood: mainly because of the challenging task of detecting atomic hydrogen in spillover systems and partly because of the inherent difficulties in accurately measuring small changes in hydrogen uptake at room temperature. In intercalated fullerides, however, the presence of metal atoms may constitute the receptor site suitable for an atomic hydrogen distribution over the receptor constituted by the fullerene molecule, available to covalently bind multiple (theoretically 60 in its complete sp^3 conversion) H atoms.

In spite of the variety of different stable structures formed by C_{60} and lightweight elements and of their outstanding capabilities of binding high hydrogen amounts, none of these structure was realized up to date. The reason is mainly that the stability of the molecule does not guarantee on the overall stability of the bulk material as intermolecular interactions and, more generally, the crystalline field, can heavily perturb the molecular stability and make it to evolve to a totally different structure (55).

1.5 Li_6C_{60} and $Na_{10}C_{60}$ as materials for hydrogen storage

Lithium intercalation in fullerides attracted considerable interest due to the massive doping levels achieved (56); only recently, however, experimental efforts were devoted to investigate the great expectation on this carbon-based material as H_2 absorbing systems. Teprovich et al. (57) explored lithium stoichiometry with a solvent assisted mixing of LiH and C_{60} synthesis and showed that Li_6C_{60} reversibly absorbs up to 5 wt% H_2 at 270 °C and 100 bar H_2 pressure. Spectrometric (TOF-MS), spectroscopic (IR and Raman) and XRD charachterization have been interpreted according to the formation of a polymeric phase which turns into a hydrofullerite *(*bcc) phase upon hydrogenation. They conclude therefore that Li atoms assist in the formation of a polymeric network that is able to expand and contract upon absorption/desorption of hydrogen and that the charge transfer from the Li atom to the C_{60} molecule results in the destabilization of the C-H bond motivating the observed lower desorption temperature, although not excluding lithium hydride formation. Similarly our group demonstrated that sodium intercalated fulleride $Na_{10}C_{60}$ can reversibly absorb up to 3.5 wt% H_2 at 200 °C and 200 bar H_2 pressure (58). Neutron and X-Rays powder diffraction were applied to probe the structural evolution upon temperature change under hydrogen pressure application. An anomalous lattice expansion was detected at 250 °C with the occurrence of NaH pattern which has been explained by partial sodium deintercalation contemporary to the formation of hydrofullerenes. This was confirmed by FT-IR transmission measurements that have shown C-H stretching vibrations absorption bands typical of covalent hydrogen-carbon bonds, thus confirming the addition of atomic hydrogen on charged fullerene molecules which explains the structural expansion. Our group observed similar results in $Li_{12}C_{60}$ (59). This relatively high lithium stoichiometry compound is able to absorb up to 4.5 wt% H_2 under 350 °C isothermal conditions and the absorption can be easily detected as a phase transition from the (*fcc*) structure the pristine sample has to the (*bcc*) structure possessed by the hydrofullerene $C_{60}H_x$. Again, FT-IR measurements demonstrated, by the observation of C-H stretching modes, that hydrogen covalent binding is accomplished by fullerenes molecules. In situ neutron diffraction explored the hydrogen desorption process and detected the return to the (*fcc*) pristine structure in a reversible storage and the contemporary thermal decomposition of lithium hydride, which is formed upon lithium de-intercalation during H_2 uptake. In both Li and Na fullerides, the presence of alkali clusters in the octahedral voids (18, 60) seems to influence the hydrogen dissociation and facilitate its chemisorption by significantly lowering the hydrogenation temperature, which is observed only at 550 °C on bare C_{60} (57). Therefore neither the Kubas, nor the electrostatic interaction seems to be the main responsible for the binding of hydrogen in Li_6C_{60} and $Na_{10}C_{60}$; however a complete understanding of hydrogen dissociation is still lacking: i.e. if H_2 dissociation is provided by intercalated ions or by charged fullerene molecules, or which is the limiting factor preventing, in both cases, a complete $C_{60}H_{60}$ hydrogenation. The present thesis is aimed to provide an answer to some of these questions.

2

Techniques for H_2 storage study

2.1 The importance of pcT and DSC acronyms

2.1.1 Manometric measurements

In view of materials application in the field of either mobile or stationary hydrogen storage, the knowledge and design of the thermodynamic properties is crucial. Pressure-concentration-temperature measurements (pcT) and differential scanning calorimetry (DSC) are the ideal tools to investigate the hydrogenation and dehydrogenation enthalpies and to determine the maximum gravimetric capacity (61). Furthermore, hydrogen sorption events can be separated and identified, as usually happens in case of different endohedral peaks in polymorphic transformations and therefore these techniques are complementary to structural investigations. The basic instrumental requirements are a precision balance (or a quartz crystal microbalance for high resolution or small samples (62)) and a programmable furnace equipped with a thermocouple to accurately monitor system temperature and its variation.

Sample is placed on a balance pan and gas pressure applied and the versatility in p, T and gas changes allows the calcultion of the H_2 mass loss/gain under a wide variety of conditions (63). Different instruments have been developed and the investigation of the hydrogen sorption properties of the materials has been carried out using the automatic *Sievert* type equipment *PCTPro2000* by *Setaram* (up to 200 bar H_2 an 450 °C). The Sievert method is based on the use of calibrated volumes to evaluate the absorbed or desorbed amount of a gas in or from a material (64). The known volumes of the sample holder and of the gas reservoir are put in communication at the beginning of the

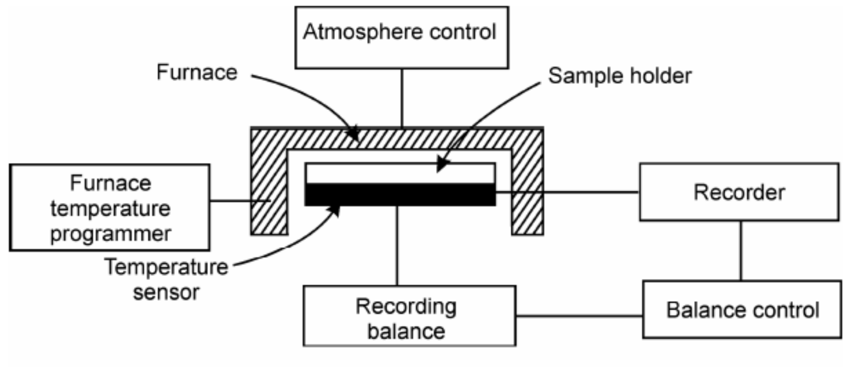

Figure 2.1: Block diagram of a thermogravimetric instrument.

measurement. The detection of temperature and pressure of the system leads to the calculation of the amount of the gas phase through an appropriate equation of state. The increase/decrease of the gas amount from the initial value is interpreted as a desorption/absorption, respectively, of the gas substance. Alternatively, flowmeters can be used to evaluate the amount of the hydrogen flown from the gas reservoir to the sample holder. By monitoring the temperature and pressure of the sample holder, the hydrogen in the gas phase is calculated and then the absorbed or desorbed hydrogen amount is obtained. It is therefore possible to keep the pressure of the sample holder strictly constant throughout the sorption test. With the *Sievert* type apparatus, both kinetics and thermodynamic measurements can be performed. Kinetic measurements are a kind of thermogravimetric analysis in which changes in physical and chemical properties of materials are measured as a function of increasing temperature (with constant heating rate) or as a function of time (with constant temperature) (65). Thermodynamic information can be also derived by Pressure-Composition Isotherms (PCIs). These pressure-composition (quasi-) equilibrium curves are obtained performing a sequence of kinetic measurements, increasing step by step the system pressure in isothermal conditions. By measuring isotherms at different temperatures and plotting the equilibrium pressure p_{eq} as a function of the inverse temperature T^{-1} the thermodynamic parameters of the de- and re-hydrogenation reaction can be determined with the Van't Hoff equation

$$\ln\left(\frac{p_{eq}}{p_0}\right) = \frac{\Delta H}{R}\cdot\frac{1}{T} - \frac{\Delta S}{R} \tag{2.1}$$

where ΔH and ΔS are the reaction enthalpy and entropy, T is the system temperature and p_{eq} is the equilibrium pressure. A pcT curve directly provide the relative mass changes allowing the quantitative estimation of involved stoichiometry. Moreover the analysis of the curve shape is used to elucidate the reaction kinetics since the temperature dependence of chemical processes may be expressed by the Arrhenius equation

$$K = Aexp(-E_\alpha/RT) \tag{2.2}$$

where K is the rate constant, R the gas constant and T the thermodynamic temperature (K). The values of the E_a and A parameters provide measures of the reaction energy barrier since they are the activation energy and the frequency factor leading the reaction respectively. The rate constant K is defined by the relationship between the rate of reaction (dα/dt) and the fraction reacted (α) according to the general relation

$$(d\alpha/dt) = k\alpha^m(1-\alpha)^n \tag{2.3}$$

It is possible to derive various sub classes of rate equation by changing the values of m and n according to different reaction models, although this is often not a straightforward path (66).

2.1.2 Differential Scanning Calorimetry

Differential scanning calorimetry (DSC) is a thermoanalytical technique in which heat capacity, latent heat, reaction enthalpies can be evaluated (67). The difference in the amount of heat required to change temperatures of a sample and a reference is measured as a function of temperature (68). The basic principle underlying this experiment is that when the sample undergoes a physical transformation such as a phase transition, heat will need to flow to it and to the reference to maintain both at the same temperature according to:

$$\Delta\left(\frac{dQ}{dt}\right) = \beta \cdot [m_s c_s - m_p c_p] \tag{2.4}$$

where the variation of heat (Q) flux is expressed in terms of masses m and heat capacities c of the sample and the reference. Whether less or more heat flows to the sample depends on whether the process is exothermic or endothermic. The result of a DSC experiment is a curve of heat flux versus temperature or versus time that can be used to calculate enthalpies of reactions through the integration of the peak corresponding to a given transition. It can be shown that the enthalpy of transition can be expressed by

$$\Delta H = K \cdot A \tag{2.5}$$

where ΔH is the enthalpy of transition, K the calorimetric constant and A is the area under the curve. The calorimetric constant depends on the instrument and can be determined by a proper calibration (69) In general, the heat in differential form measured in a calorimeter can be written

$$dQ = \left[\left(\frac{\partial H}{\partial p} \right) - V \right]_{T,\xi} dp + \left(\frac{\partial H}{\partial T} \right)_{p,\xi} dT + \left(\frac{\partial H}{\partial \xi} \right)_{p,T} d\xi - \sum dE_i \tag{2.6}$$

where the enthalpy H is a function of the pressure p, temperature T, and composition ξ and E_i represents contributions from all other energy forms (e.g surface heat). When measuring some materials (e.g. metal hydrides) in isothermal mode the first and second terms can be considered zero (70). Equation 2.5 therefore simplifies to the lone concentration dependent term and consequently the integrated value in the DSC curve corresponds to the enthalpy of the hydrogenation reaction. Combination of both thermogravimetric and calorimetric measurements has the great advantage of being able to correlate both mass variation and energy on the same sample.

2.2 The ball milling technique

The ball milling method is used to grind materials for different purposes and applications (71, 72, 73) The material to be ground is inserted inside the milling vial together with the milling media, which most commonly are balls or shots. The mill motor and driving components produce the vial motion, which causes crashes between the milling media and the material to be treated. The purpose of the ball milling is the reduction of particle size of the ground material together with the uniform mixing. However other processes, either wet (if some solvent is present in the vial) or dry synthesis, or mechanical alloying, can occur due to the loca high temperature condition realized in high energy collisions (74). Depending on the movement that the milling vial is subject to, there are different type of mill producing specific features material since the vials walls and the balls creates a combination of forces, compression and shear, which shape particles in size and kind. Shakers and vibrator mills are both indicated as high efficiency mills, due to the fine pulverization they assure if compared to other types of mill (75). Planetary mills use rotation to generate the movement and, in addition to rotation around the vial axis, a revolution motion is added in the opposite direction. Higher temperatures than the ones obtained in vibrating-type can be achieved (76). With high energy ball milling non-equilibrium processes (e.g. mechanical alloying) can occur, allowing the formation of metastable phases, which cannot be synthesized by conventional ways (77). It is also possible to realize the milling process in a hydrogen atmosphere inside the milling vial (reactive milling process). In this synthesis, temperatures achievable together with the exothermic effect of H_2 absorption reaction must be considered in order to avoid overpressure inside the chamber. The temperature raising can be controlled by using refrigeration systems, or by alternating milling and pause intervals.

2.3 Muon Spin Resonance: a very general introduction

A form of magnetic resonance known as μSR has nowadays widespread use in condensed matter physics and materials science (78). The success of the μSR techniques relies on two circumstances: the intrinsic polarisation of the muons and the anisotropy of the positron emission in their subsequent decay. Such characteristics provide μSR the unique sensitivity to weak internal magnetic fields (10^{-5} T), the possibility to probe local hyperfine interactions and insensitivity to impurities since the signal amplitude is proportional to the volume fraction. The probe in this technique is the spin of the muon (79), a short lived elementary particle which is produced in pion decay process

$$\pi^- \rightarrow \nu^- + \bar{\nu}_\mu \quad \pi^+ \rightarrow \nu^+ + \bar{\nu}_\mu \tag{2.7}$$

and collected to create a completely spin polarised beam of positive charged particles (80). Muons are then implanted in matter where they face a thermalisation process. It lowers their kinetic energy from the Mev range they possess after the beam formation to the keV range after atoms ionisation and scattering with electrons and, later, to the eV range after successive electron capture and loss events. An electron capture by a muon leads to the formation of muonium, a light isotope of hydrogen (the muon mass is 1/9 of the proton mass, see Fig 2.3 for a picture) chemically equivalent to it (81). Such a phenomena makes μSR technique useful even to highlight hydrogen behaviour in materials (82, 83). After muonium formation during thermalisation process its energy is furtherly reduced by muonium-atoms collisions which lead to a thermalised muonium. This is usually stabilized in insulating materials while it undergoes dissociation process producing free thermalised muons in conductive materials. Once muons are implanted within a sample their local magnetic environment dictates the subsequent evolution of their spin vectors. If they experience magnetic fields, as well as their time or spacial variations it is reflected in a dephasing or depolarisation of the spin ensemble. The information on the local environment is delivered at the end of the mean muon lifetime (2.197 μs) in the form of a positron emitted in the muon spin direction at the instant of its decay

$$\mu \rightarrow e^{+} + \nu_e + \bar{\nu}_\mu \tag{2.8}$$

. Unfortunately positrons are not precisely emitted along the muon spin direction but distributed according to the probability function

$$W(\Theta) = 1 + a \cdot cos(\Theta) \tag{2.9}$$

where Θ is the angle between the muon spin and positron emission and $0 \leq a \leq 1$ is the asymmetry factor depending on the positron energy. A correct integration over the energy dependent probabilities of positron emission and detection leads to the evaluation of the decay asymmetry or polarization, an experimental parameter given by the equation

$$P(t) = \frac{F(t) - \alpha B(t)}{F(t) + \alpha B(t)} \tag{2.10}$$

where F and B are forward and backward time dependent positron detector countrates (with respect to the beam polarisation direction) (84) and α is the detector asymmetry, a correction applied to take into account any deviation from the ideal geometrical experimental setup. The extraction of a time dependent muon polarisation and its interpretation are usually the goal of a muon spin experiment since embody detailed information on the spatial distribution and dynamical fluctuations of the local magnetic environment. A general scheme of a μSR experiment is reported in figure 2.2.

2.4 The Muon fate into the Matter

The two most common experimental configurations used in μSR experiments are the transverse field (TF) and longitudinal field geometry (LF or ZF if no magnetic field

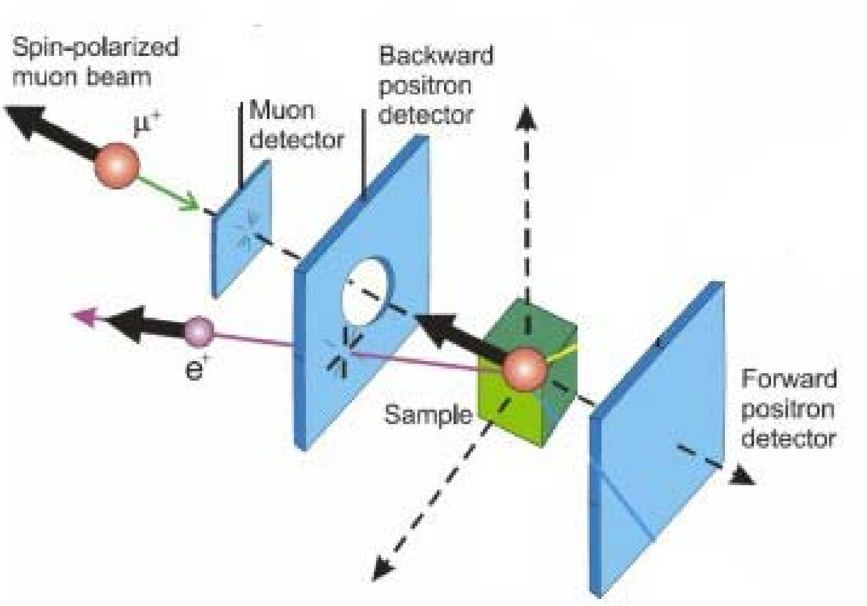

Figure 2.2: ZF-μSR experiment schematic representation. The detectors are organised in two groups, forward and backward

is applied), The former consists in the application of a magnetic field H in a direction perpendicular to the muon polarization. μ^+ spins are forced to precess around this with their Larmor frequency

$$\omega = \gamma_\mu H \tag{2.11}$$

where γ_μ is the muon magnetogyric ratio and thus an oscillating signal is observed in the asymmetry. In the latter the external field is applied along the same direction of the muon spin and added to the local fields. Such an experiment provides a view of the magnetic environment found by the muon after its implantation. Three special cases allow the observation of a single frequency coherent oscillation: the first one is the presence of a constant and uniform local field within the sample, as in the case of a long range magnetic order (85, 86). The second one happens if paramagnetic muonium is stable in the sample: In this case the muon senses the hyperfine interaction due to the bound eletron and its energy is described by the hamiltonian

$$H/\hbar = -\gamma_\mu I \cdot B + \gamma_e S \cdot B + AS \cdot I \tag{2.12}$$

where **B** is the applied magnetic field, **A** is the hyperfine coupling constant and **I** and **S** the muon and electron spin respectively. The last possibility is the formation

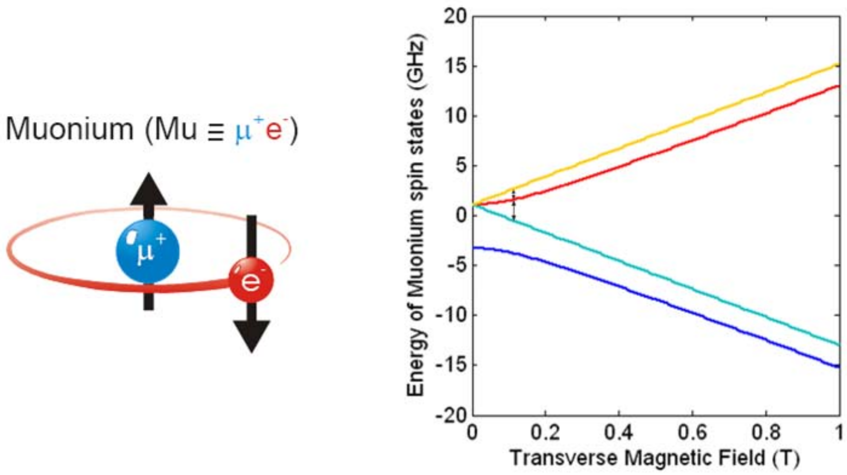

Figure 2.3: Left: a simple picture of Muonium. Right: the Breit-Rabi diagram for free Muonium in vacuum: the plot shows Muonium spin energy levels as a function of the applied transverse magnetic field. In a low TF (a few Gauss) is possible to observe the two nearly degenerate transitions among the triplet states, highlighted by the black arrows

of muonium-substituted radical species. Muonium undergoes an addition reaction in which it gets covalently bound to unsaturated systems, thus miming hydrogen addition. The last two cases show a relatively high precession frequency (typically more than few hundreds kHz) which may fall out of the spectrometer bandwidth like in case of pulsed muon sources (ISIS-Rutherford Appleton Laboratory i.e.) giving rise to a lack of asymmetry usually called ”missing fraction”. The radical formation can be verified either by the application of a small TF (2 G), which is expected to induce transitions among the muonium triplet states (see Fig. 2.3), or by asymmetry measurements as a function of an applied longitudinal field (LF), which allow to observe the repolarization of the initial asymmetry (87).

In most situations, on the contrary, a relaxation of the muon polarization is expected. The simpliest case is provided by the muon stopping in an electrostatic equilibrium position and experiencing randomly oriented dipolar fields (whose average is zero) from neighbouring electrons and nuclei. Such a situation is usually described by a Gaussian (under the approximation of relatively high concentration (88)) or Lorentzian (in the approximation of dilute spin system (89)) static field distribution. Such an environment affects the polarization which follow the gaussian or lorentzian Kubo-Toyabe function (90, 91):

$$P(t) = \frac{1}{3} + \frac{2}{3}(1 - \sigma^2 t^2) \exp^{-\sigma^2 t^2/2} \quad P(t) = \frac{1}{3} + \frac{2}{3}(1 - \lambda t) \exp^{-\lambda t} \tag{2.13}$$

where the relaxation rates σ and λ describe the width of the local field distribution function at the muon site (92, 93). If muons are subject to diffusive dynamics or if static muons sense fluctuations in local fields in the strong collision approximation (extreme motional narrowing regime) the resulting relaxation function can be simplified to a Lorenztian form. These paragraphs are only meant to provide an introductory reading to the μSR technique. More exhaustive and detailed treatments may be found in subject related textbooks such as Abragham, Slichter and Schenck's (92, 94, 95) or in review publications (96, 97, 98).

3

Materials & Experimental methods

3.1 Intercalated Fullerides for μSR measurements

In order to prepare Li_6C_{60}, stoichiometric amount of Lithium metal (Sigma Aldrich, 99% purity) was mixed with C_{60} (MER, 99.95% purity) through high energy ball milling. Sample was then heat-treated at 270 °C for 24 hours to improve cristallinity. $Na_{10}C_{60}$ was synthesized accordingly to (58) from a 350 °C heat treatment of a stoichiometric mixture of fullerene and sodium azide powders. The air sensitivity of the samples required to operate under strict oxygen and moisture free condition (glove box under argon atmosphere with less than 1 ppm O_2 and H_2O). Powder diffraction investigation confirmed the expected *fcc* crystal structure for both Li and Na fullerides. Unlike many other fullerides the presence of large intercalated clusters hinders the fullerene rotational disorder and therefore C_{60} molecules are blocked (18). Hydrogenation was carried on at a temperature of 350 °C and a H_2 pressure of 100 bar. Sievert (PCT) measurements, performed in a manometric instrument PCTPro2000 by Hy-Energy& Setaram, confirmed already reported uptake amount of 5 wt% (57) for Li_6C_{60} and 3.5 wt% (58) for $Na_{10}C_{60}$. The estimated amount of hydrogen chemisorbed on C_{60} is $C_{60}H_{40}$ and $C_{60}H_{34}$ respectively.

3.2 Transition metal addition to fullerides

3.2.1 Alloys of Platinum & palladium

Only Li_6C_{60} was selected for further improvement since its storage final value (57) exceeds the one reported in sodium fullerides (58) and it is therefore the most promising for storage purposes. Since binary phase diagrams predict platinum and palladium solubility in lithium for a wide compositional range (99, 100) and since these transition metals possess catalytic activities toward hydrogen (101) they were selected for the decoration of intercalated lithium fullerides. Different Li-platinum and Li-palladium alloys were prepared through the addition of lithium metal (Sigma Aldrich, 99%) and platinum (Sigma Aldrich, 99.99% in weight percentage equal to 15, 25, 35, 50, 65%) or palladium (Sigma Aldrich, 99.98% in weight 15, 25, 35, 45, 55, 68%) in tantalum cylinders which were sealed in glass vials under 1 mbar He atmosphere. These vials were treated for 2.5 hours at 400 °C and then cooled down to room temperature. This treatment was meant to prepare a segregation of Li_9Pt and Li_5Pd alloys (in final different amounts) in lithium matrix which would have been used as decoration reagent. Alloys were cut in ribbons and joined to fullerene powder (MER 99.9%, further purified in vacuum at 250° C for 12 hours) in an high energy ball milling (Mini-Mill Pulverisette23-Fritsch) where they were mixed at 30 Hz frequency for 30 minutes which were divided in 10 minutes turns, each separated by 5 minutes cooling. Transition metal decorated lithium intercalated fullerides corresponding to stoichiometries $Li_6Pt_xC_{60}$ (x=0.03, 0.07, 0.11, 0.26, 0.42) and $Li_6Pd_yC_{60}$ (y=0.07, 0.13, 0.21, 0.8) were prepared. The air sensitivity of both $Li_6Pt_xC_{60}$ and $Li_6Pd_yC_{60}$ samples required their conservation under strict oxygen and moisture free condition (Ar glove box with less than 1 ppm O_2 and H_2O atmosphere).

3.2.2 A way to add other transition metals

Binary phase diagrams do not often predict solubility with lithium, in case of transition metal ions. This is the case of nickel and titanium, which are both predicted suitable hydrogen binders (43, 45) since forming H_2 stabilizing orbital interactions. However transition metal alogenides are commercially available. In order to achieve Ti/Ni decoration of lithium fullerides, a synthetic strategy based on the application of a solid state metathesis reaction involving the intercalated alkali metal was applied as:

$$Li_6C_{60} + xMeCl_n \rightarrow Li_{6-nx}C_{60} + xMe + nxLiCl \tag{3.1}$$

Since platinum and palladium decoration obtained the higher final uptake results in a relatively low stoichiometric range, x=0.11 was selected in order to gather a direct comparison of the efficiencies in case of different ions. Stoichiometric amounts of lithium metal (Sigma Aldrich, 99%) were joined to fullerene powders (MER 99.9%) in high energy agate ball milling (Mini-Mill Pulverisette23-Fritsch) and mixed for 10 minutes at 30 Hz frequency. After this preliminary mixing, stoichiometric amounts of transition metal chlorides were added to the powders ($NiCl_2$, $PdCl_2$, $TiCl_2$ and $CeCl_3$ were used) and further milled twice at 30 Hz for ten minutes separated by 5 minutes cooling.

3.2.3 Nickel clusters: transition metal particle size control

Since SEM characterization showed a transition metal particle size distribution and since absorption measurements suggest that a surface catalytic activity is promoted in decorated lithium fullerides, as it will be described later, it become necessary to gain control over the size of nickel aggregates to further improve these materials. The synthesis described in the previous paragraph is not suitable for this purpose since limited by the particle size reached during the high energy ball milling. A suitable source of nickel was selected in the metal-carbonyl clusters $(NBu_4)[Ni_6(CO)_{12}]$ and $(NEt_4)_3[HNi_{12}(CO)_{21}]$ (102, 103), which are known to decompose at the relatively low temperatures of 150 °C. Our attention was focused on the Ni stoichiometry x=0.11 because data obtained through the pcT study of nickel stoichiometries revealed $Li_6Ni_{0.11}C_{60}$ as the most promising system with respect to hydrogen absorption. Two different strategies were adopted: in the former a stoichiometric amount of metal-carbonyl cluster powder was added to lithium (Sigma Aldrich, 99%) and C_{60} powders (MER 99.9%) in high energy ball milled. Probably the local high temperatures reached in this mechanical mixing resulted sufficient for the decomposition of the nickel precursor and clusters aggregation; as a consequence, the presence of metal particles, even visible by eyes, was detected. In order to prevent any cluster aggregation the latter synthesis was developed: nickel was introduced with a soft grinding addition. Li_6C_{60}

was synthesized in high energy ball milling (30 Hz, 30 minutes mixing) and the resulting powders were hand-ground together with stoichiometric amounts of Ni clusters (x=0.11).

3.3 Characterization methods

Hydrogenation studies were performed on the as prepared samples in the PCTPro-2000 manometric instrument by Setaram by heating them (about 200 mg each sample) from room temperature to 350 °C at 5 °C/min under 100 bar H_2 and appending an isotherm of 10 hours. A portion of the discharged powders was analysed by coupled calorimetric manometric measurements by connecting the PCTPro to the Setaram Sensys high pressure DSC cells by stainless steel high pressure tubes. The charged powders (about 20 mg) were heated from room temperature up to 380 °C under 0.5 bar H_2 at 5 °C/min and the kinetic and calorimetric signals were recorded simultaneously. Pure Li_6C_{60} sample was analysed in the same conditions as a reference. Scanning electron microscopy was performed on both the as prepared and the hydrogenated samples (without gold sputtering) by the Zeiss EVO-MA10-HR microscope. To avoid air exposition of the samples, a home-made sealed sample holder has been used in order to transfer samples from the glove-box in the SEM analysis chamber under vacuum. For TEM analysis, a small amount of sample was exposed to air and dispersed in cyclohexane. The suspension was sonicated for a minute and, then, a droplet was deposited onto carbon coated copper grids. High Resolution Transmission Electron Microscopy (HRTEM) and High Angle Annular Dark Field (HAADF) Scanning Transmission Electron Microscopy (STEM) were carried out on a JEOL JEM-2200FS microscope with a Schottky gun working at 200 kV (HRTEM point resolution 0.19 nm, STEM nominal probe size 0.5 nm), equipped with an in-column energy filter (Ω-type), a CCD high resolution camera and STEM detectors. The morphology and structure was determined by High Resolution Transmission Electron Microscopy (HRTEM) and by High Angle Annular Dark Field (HAADF) Scanning Transmission Electron Microscopy (STEM). Micro-Raman measurements were carried out using a Labram Dilor Raman H10 spectrometer equipped with an Olympus microscope HS BX40 objective and with a cooled CCD camera as photodetector. The 632.8 nm light from an HeNe laser was used as the excitation radiation. The nominal spatial resolution is given by the beam diameter at the focal plane, and depends on the diameter of the main diffraction spot (1.22 λ/NA), where λ is the laser wavelength and NA is the numerical aperture of the objective. A 100x lens was normally used, with a spatial resolution of 1 μm A quasi-confocal geometry was achieved with slits and confocal hole apertures kept at 200 μm, leading to a depth resolution of 2 μm. A grating with 1800 grooves/mm was used. The samples were sealed in glass capillaries with a diameter of 0.7 mm and a wall thickness of 0.01 mm and were mounted on the motorized xy stage of the microscope, and all the measurements were performed at room temperature. X-Ray powder diffraction analysis was performed by either Bruker D5005 or Bruker D8 diffractometer (Cu Kα radiation) by using a suitable, sealed zero background sample holder in Bragg-Brentano geometry on the first instrument and sealed glass or quartz capillaries (0.7 mm diameter and 0.1 mm wall thickness) in Debye-Scherrer geometry on the second diffractometer. Zero and longitudinal magnetic field μSR spectra were collected on the EMU spectrometer at the ISIS-Rutherford Appleton laboratory. Samples were set in Ag coated aluminium cells and sealed with kapton windows. The full polarization measurement was carried on in a transverse field experiment on a reference silver plate. Nuclear magnetic resonance studies have been performed on ^{7}Li nuclei with Apollo Techmag spectrometer and Kalmus amplifier at 132.1138 MHz operative frequency.

4

Results & Discussion

4.1 The muon answer on the hydrogenation mechanism

4.1.1 Zero and Longitudinal field relaxation.

As shown in the previous chapters very little is known on the mechanisms driving the H_2 absorption in fullerides, but a more detailed understanding of the process is fundamental to further improve the capabilities of this new class of H_2 absorbing materials. Only few experimental techniques are suitable to provide informations on the dynamical evolution of H_2 within a material: among them, μSR has been extensively used to probe the internal magnetic field distribution and the induced electronic states both in C_{60} and in fullerides. Usually, in these materials, different muon environments can be observed: muons can stay as free unbound particles (diamagnetic muons), they can bind to electrons forming muonium (104, 105) which is only observed endohedrally in fullerides or they can promote the formation of muon adduct radicals in which Mu chemically reacts with the C_{60} molecule (106). Only in pristine C_{60} all the three fractions are present (104), while in metallic fullerides, such as A_3C_{60}, the formation of muonium is prevented by the conduction electrons screening the muon Coulomb field (107). The ionic character of the other insulating alkali fullerides also prevents the formation of Mu (13). The situation that is met in these particular fullerides which effectively work for hydrogen storage purposes is definitively different from the one commonly known. Both pristine and hydrogenated Li_6C_{60} and $Na_{10}C_{60}$ zero field μSR spectra reported in Fig. 4.1 show two different components: a slowly decaying fraction fitted with different decay functions (see caption in Fig. 4.1 for more details) plus an

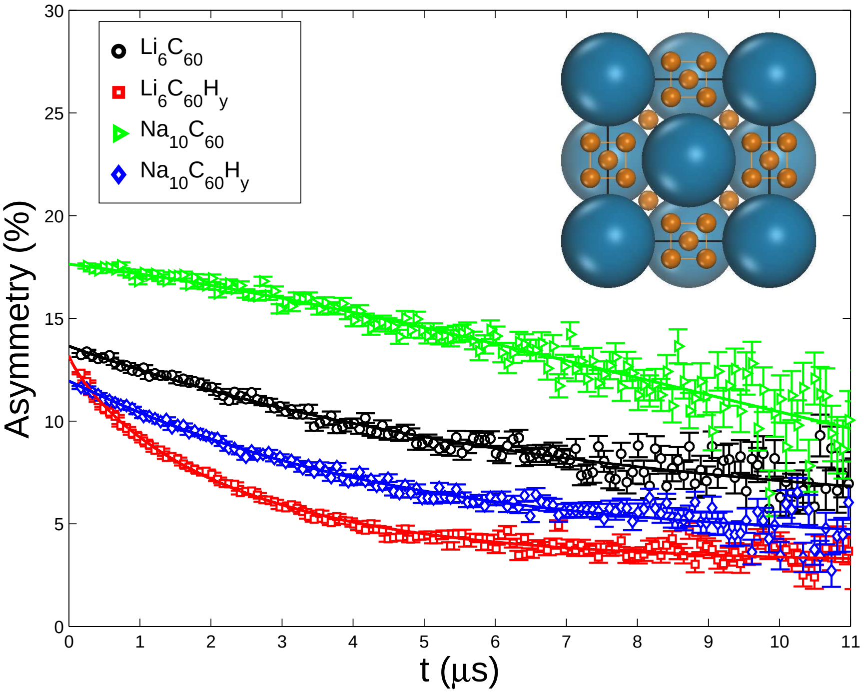

Figure 4.1: Zero field muon spin relaxation in pristine and hydrogenated Li_6C_{60} and $Na_{10}C_{60}$ at 5 K. Fitting curves are reported as solid lines. Li_6C_{60} and $Na_{10}C_{60}H_y$ data have been fitted with a lorentzian decay, $Na_{10}C_{60}$ with gaussian and $Li_6C_{60}H_y$ according to a stretched exponential lineshape. Inset picture shows schematic *fcc* structure of cluster intercalated fullerides.

evident missing fraction which reduces the initial asymmetry of the histograms to a value smaller than the instrument full one (22.6%).

The presence of a missing fraction indicates that some muons precession frequency exceeds the instrument pass-band (ν_{max}=13 MHz). In absence of magnetic phenomena, this is the signature of hyperfine interaction of μ^+ with an unpaired electron either in isolated muonium or in a muon substituted radical in case of Mu chemisorption on C_{60}. The hyperfine coupling between the muon and the paramagnetic electron can be estimated by the field dependence of the initial muon polarization. In case of isotropic coupling (as in free muonium) the initial polarization goes from 50% at zero field to 100% at high fields which fully decouple the muon and the electron. The functional behaviour has the form (92):

$$P = \left[1 + \frac{x^2}{x^2+1}\right] \cdot \frac{1}{2} \tag{4.1}$$

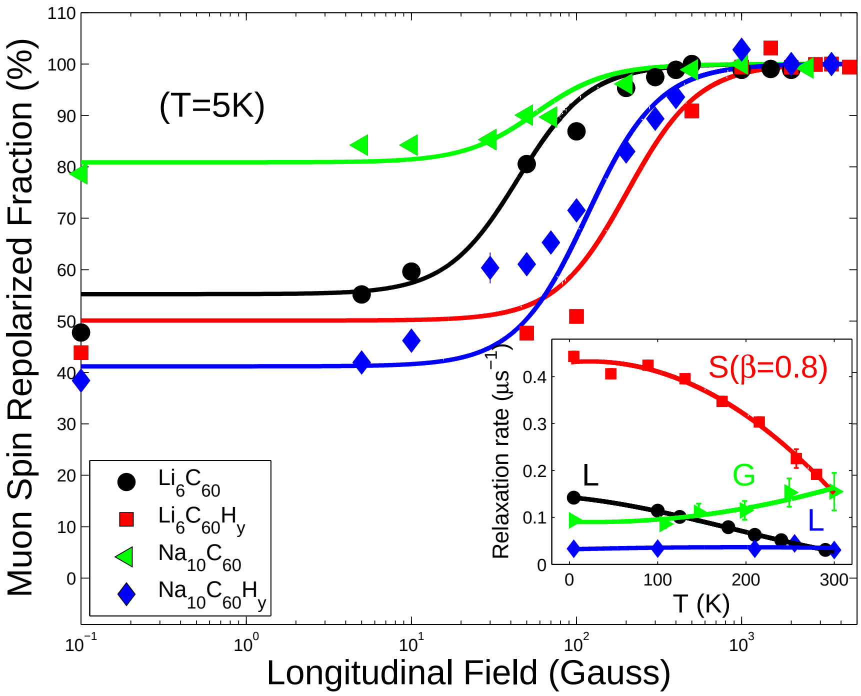

Figure 4.2: Muon spin repolarization experiment in pristine and hydrogenated Li_6C_{60} and $Na_{10}C_{60}$. The repolarized asymmetries have been fitted (here shown by solid lines) with equation 4.2 (92). The inset reports the temperature evolution of relaxation rate. Letters are reminder of ZF-relaxation fitting with gaussian (G), lorentzian (L) or stretched exponential (S) functions and solid lines are guides to the eye.

where x is the ratio of the applied field to the hyperfine field. The latter is 1580 G for the free muonium while a considerable lower value is expected for adduct radicals. In case of anisotropic hyperfine interaction (like it is observed in most of the radicals), the zero field polarization is quenched from 50% to zero and equation 4.1 assumes an approximate form $P = x^2/1 + x^2$ (108). The repolarization of the muon spin for the four different samples is shown in Fig. 4.2 in which it is evident that the application of 1 kG is sufficient to fully repolarize the missing asymmetry, while a polarization recovery at 1.58 kG is not observed, thus excluding the presence of free muonium.

This demonstrates that missing fraction is due to the formation of radicals while no endohedral muonium is produced (96). The reaching of 100% repolarization in Fig. 4.2 at the highest applied longitudinal field moreover guarantees that no other muon thermalization process contributes to the observed missing fraction. The repolarization curves have been tentatively fitted with the function

$$P_{exp} = P_{diam} + A_{rad} \cdot \left[\frac{x^2}{x^2 + 1} \right] \tag{4.2}$$

where P_{diam} is the fraction of diamagnetic muons observed in zero field experiment and A_{rad} is the amplitude of the radical fraction. The fit to function 4.2 allows just an estimation of the average hyperfine field as the known anisotropic character of the hyperfine coupling in C_{60} and the presence of several non equivalent carbons in the crystal structures probably do not allow a more precise measurement of the coupling parameters in an experiment on powders. It was found that in Li_6C_{60} radical hyperfine frequency rises from a value of 123(19) MHz in pristine sample to a value of 550(30) MHz in hydrogenated sample; in $Na_{10}C_{60}$ it rises from 158(22) MHz to 325(27) MHz in the hydrogenated sample.

4.1.2 Temperature evolution and Interpretation

The complex scenario depicted by the μSR experiment is helpful to better understand the hydrogenation process in alkali intercalated fullerides. In such systems, sizeable hydrogen storage with reversible character is reached through the hydrogenation of the C_{60}^{n-} molecule at much milder conditions as compared with those necessary in pristine C_{60} to achieve the $C_{60}H_y$ hydrofullerite. This can be explained as due to the catalytic effect of the intercalated alkali clusters, effective in the dissociation of the hydrogen molecule and to the subsequent migration of the hydrogen atoms from the metallic clusters to the buckyball (58). The slowly decaying component (diamagnetic muon fraction, P_{diam} in eq. 4.2), is due to the dipolar interaction of muons with Li or Na nuclear moments in pristine samples and to the additional dipolar interaction with hydrogen in hydrogenated compounds. This effect is clearly observed in lithium compounds while the opposite behaviour happens in sodium samples as a consequence of a different dinamical regime. The fitted lorentzian (or stretched exponential) depolarization functions, which are shown for pristine and hydrogenated Li_6C_{60} are attributed to muons diffusing interstitially through the clusters; in the case of $Na_{10}C_{60}$, a gaussian relaxation witnesses the absence of any diffusive dynamics, supplying a larger decay rate in pristine sample. The different fitted decay rates and their temperature dependence (see inset in Fig. 4.2) are indicative of various diffusing regimes. It is difficult, in this case, to assign this diamagnetic fraction to bare muons or to Mu^-, whose formation is commonly observed in alkali metals hydrides (109), but other decay mechanisms like spin exchange can be ruled out in our systems where no paramagnetic centers are present. Both Li_6C_{60} and $Na_{10}C_{60}$ are indeed diamagnetic materials and the charge transfer from the cluster to C_{60} is probably of 4 electrons in Li_6C_{60} and of 6 electrons in $Na_{10}C_{60}$ (60). In the former case, the Jahn-Teller splitting of the t_{1u} LUMO of C_{60} gives rise to singlet states even in the case of partial filling (110).

The fraction of adduct radicals produced is larger in hydrogenated samples than in the pristine ones, as shown in Table 4.1.

	Li_6C_{60}	$Li_6C_{60}H_y$	$Na_{10}C_{60}$	$Na_{10}C_{60}H_y$
5K	58%	61%	32%	66%
290K	23%	39%	22%	54%

Table 4.1: Radical fraction percentage relative to full asymmetry in pristine and hydrogenated samples.

This can be rationalised by taking into account that the presence of local curvature in carbon based nanostructures has promoting effects on the H_2 binding energy and that H binding is shown to increase on sp^2 receptors (33), like graphene, by increasing the H coverage (111). In the present case the curvature of partially hydrogenated fullerene cage is clearly greater than in bare C_{60}, due to the presence of purely sp^3 hybridised carbon atoms (112).

The hyperfine field on the muon can be interpreted as an average value of the electron density sensed by the muon in the radical state. Although the extracted values were obtained under the assumption of pure isotropic hyperfine coupling, they could still be interpreted on the basis of the consideration that, in pristine Li_6C_{60} and $Na_{10}C_{60}$, the hyperfine coupling was found to be significatively lower than in pure C_{60}. Here, the presence of C_{60}^{n-} anions, in which the t_{1u} molecular orbital is almost completely filled, allows to efficiently delocalise the further radical electrons, and hence to decrease the hyperfine interaction. As a matter of fact, it is known that light alkali metals intercalated in fullerenes only partially donate their charge to C_{60} (113). On the other hand, after the hydrogenation, the conversion to sp^3 of part of carbon atoms on the fullerene cage deeply affects the electronic arrangement of the molecule; this

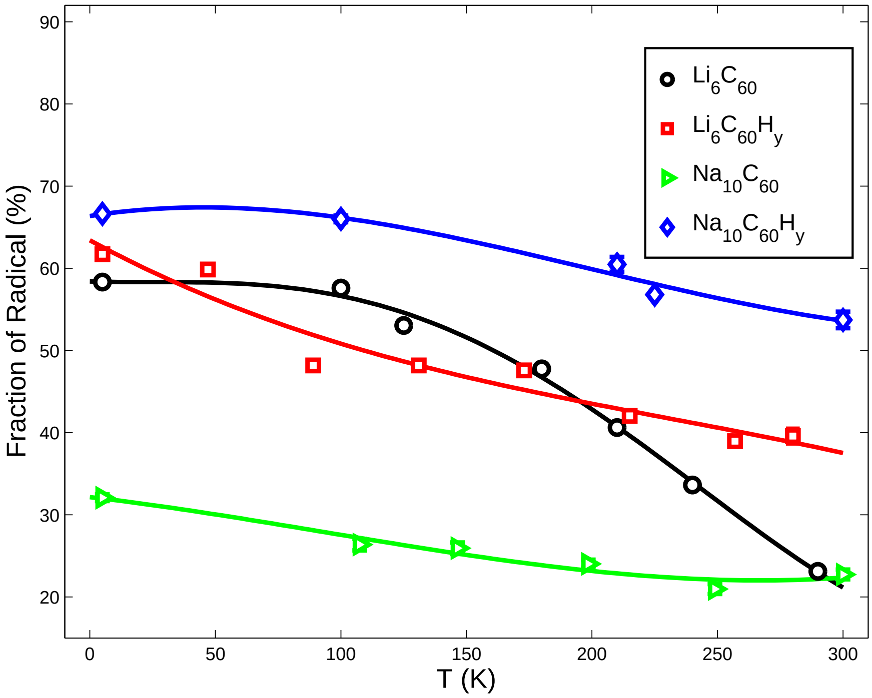

Figure 4.3: Temperature dependence of the fraction of muons producing a radical obtained as difference between full asymmetry and fitted zero field initial asymmetries (A_{rad} in eq. 4.2); solid lines are a guide to the eye.

induces the localization of the paramagnetic electrons, thus also increasing the muon hyperfine coupling.

The presence of muon adduct radicals in intercalated fullerides is itself remarkable as it proves that their absence in other known fullerides is probably due to the lack of intestitial Mu (although present endohedrally), and not to the instability of radicals in charged C_{60}, as previously thought (107). Unlike the most common alkali intercalated fullerides, in these systems the intercalation of partly ionized alkali metal clusters (18, 60) is probably at the origin of the observed peculiar behaviour: the delocalized electrons residing on clusters can be captured by the muon forming muonium. Surprisingly, differently to what observed in pure C_{60} (114), the fraction of radicals here depends on temperature. Fig. 4.3 shows the temperature dependence of the observed missing fractions which were found to invariably increase on cooling for all the investigated samples.

Such a behaviour indicates that the mechanism of atomic hydrogen capture by C_{60}^{n-}

which forms hydrofullerite is already efficient at room temperature and increased at cryogenic T. This suggests that also hydrogen absoption is expected to be enhanced at low T, as long as atomic H is available, while the high temperatures required for H_2 absorption appear to be necessary for the catalytic dissociation of the H_2 molecule mediated by the intercalated alkali clusters. These results, therefore, suggest that in order to increase the storage capabilities of these materials, the assisted dissociation of the H_2 molecule must be improved. A possible way to achieve this is the addition of transition metals, which are known to efficiently catalyze the H_2 dissociation (101). However, as experimentally proved (115), the simple intercalation of transition metal atoms is not sufficient to reach the high uptake rates observed in $Na_{10}C_{60}$ and Li_6C_{60}, as the charged state of C_{60}, not achieved in transition metals intercalated fullerides, appears to have a promoting role in the induction of an high hydrogenation degree.

4.2 H_2 storage in platinum and palladium decorated Li_6C_{60}

Consequently to the results of the previous section in this part we detail the properties of hybrid transition metals lithium fullerides. Since Li_6C_{60} final storage value (57) exceeds the one reported in sodium fullerides (58) this material was selected for further improvement with the addition of transition metals such as platinum and palladium. These metals, which were chosen as doping metals for their renown heterogeneous catalysis (52), were introduced from lithium-TMs alloys as described in chapter 3.

4.2.1 Structural Investigation

Two transition metal decorated lithium intercalated fullerides were selected for X-ray powder diffraction on the basis of their absorption values: pristine and hydrogenated $Li_6Pt_{0.11}C_{60}$ and $Li_6Pd_{0.07}C_{60}$ were analysed. The former, which is reported in figure 4.4 shows the presence of a majority phase Li_6C_{60}, accounting for the most intense peaks in the range 2Θ=10-40°.

Peaks of this phase appear broad, but they can be easily indexed with the monoclinic cell isostructural to Li_4C_{60} polymer (117), plus an *fcc* monomer phase belonging to the lithium intercalated fulleride. At higher angles, two broad reflections, respectively at $2\Theta=40.7°$ and $2\Theta=47.4°$, witness the presence of Pt particles, which segregates during the synthesis procedure. The expected position for the reflection (1 1 1) of Pt is

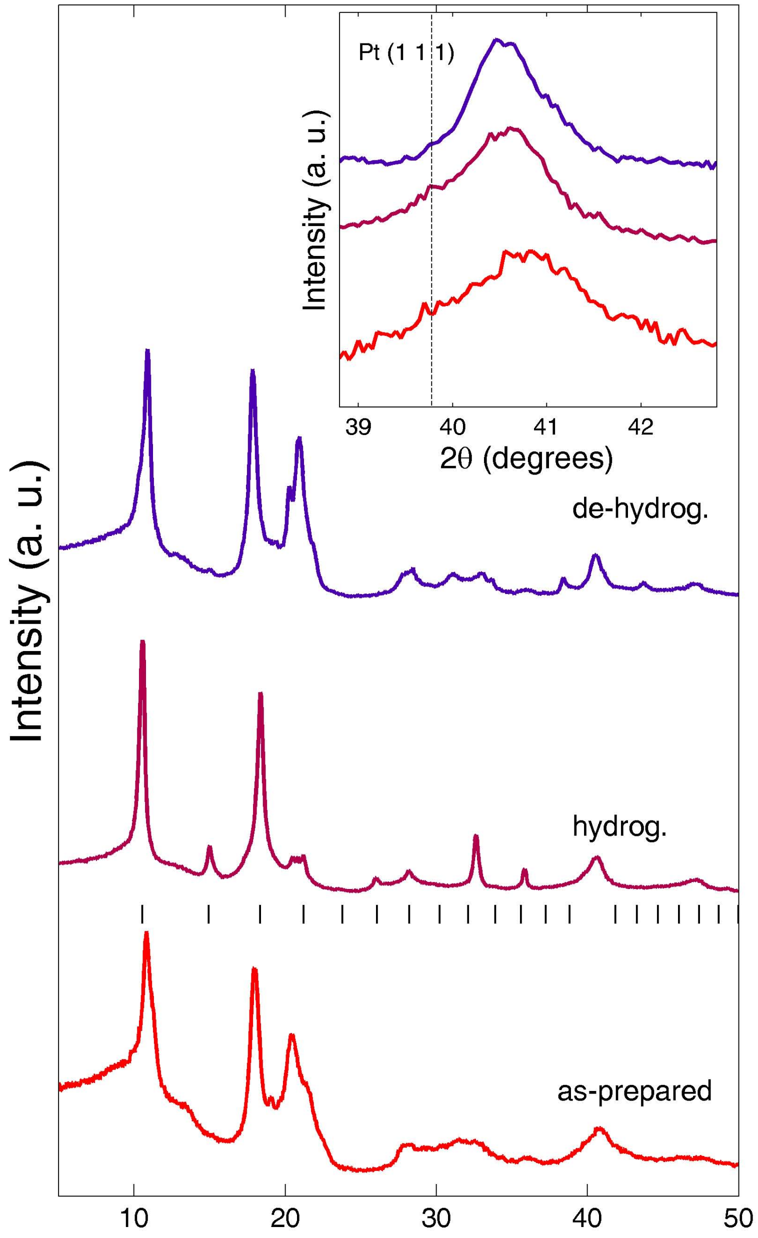

Figure 4.4: X-ray diffraction profiles of $Li_6Pt_{0.11}C_{60}$ collected on the as-prepared sample (red line), on the sample after hydrogenation (purple line) and after de-hydrogenation (blu line). The black ticks mark the reflection positions of the hydrofullerite $C_{60}H_{36}$ (see text), accordingly to (116). The asterisk indicates a reflection which was tentatively attributed to graphite. Inset: evolution of the peak at 2Θ=40.7°, ascribed to the presence of Pt nanoparticles. The dashed line indicates the expected position for the (1 1 1) reflection of Pt.

at 2Θ=39.8° (118) and the rather large upshift of this reflection is not yet completely understood, although the strong reduction of the size of the nanoparticles (see below) could account for a sensitive contraction of the Pt cell dimension. A crude estimation of the particle size can be obtained from the broadening of the X-ray reflection by the Scherrers formula p=K·λ/(b·cos(θ)), (where λ is the radiation wavelenght, b is the broadening of the peak and K is the Scherrer constant and was assumed 0.90, as originally proposed by Scherrer (119)). The average size of the crystallite (p) is defined as the cube root of the volume of particle. The fit of the (111) peak gives an average diameter of 4 nm, a value much smaller than the dimensions of Pt clusters seen in the scanning electron microscopy (SEM). This suggests that the metal aggregates visible by SEM are composed of smaller crystallites. After the treatment under hydrogen at high temperature (intermediate diffractogram in 4.4), the majority of the sample takes a *bcc* crystalline arrangement (a=11.83(3)$\dot{A}$). The same structure was observed in the hydrofullerene $C_{60}H_{36}$ (116). The loss of the C_{60} I_h icosahedral symmetry in $C_{60}H_y$ molecules makes the *bcc* arrangement energetically favorable with respect to the *fcc*. The peaks of metal Pt are still present in the hydrogenated sample, while no PtH_x phase was observed. In this case (see inset in Fig. 4.4) a new narrower peak is present nearby the broad peak observed in the as-prepared sample, whose position is in very good agreement with Pt (1 1 1) reflection. This indicates that a partial aggregation of Pt nanoparticles is induced with the high temperature reached during hydrogenation. Some small peaks of the diffractogram were indexed with the *fcc* cell of pristine C_{60} (S.G.: Fm-3m, a=14.16$\dot{A}$), corresponding to roughly 5 wt% in mass of the sample and indicating that the H treatment was not effective to hydrogenate the whole fullerene molecules. The transition from the lithium fulleride polymer to its monomer *Fm-3m* phase is known (120) to take place at the temperature reached during hydrogenation isotherm (590 K), thus increasing sample homogeneity. After the de-hydrogenation, the sample recovers the original structure with an increase in the monomer phase, confirming that the hydrogenation process of the fullerene molecules is reversible (see Fig. 4.4). After de-hydrogenation, the peak of metal Pt again appears upshifted and broader, indicating a clear structural activity of Pt in hydrogen absorption and desorption. X-ray diffraction data collected on $Li_6Pd_{0.07}C_{60}$, reported in Figure. 4.5 indicate that in the as-prepared sample only the Li_6C_{60} phase is present, while no evident traces of Pd segregation are evident.

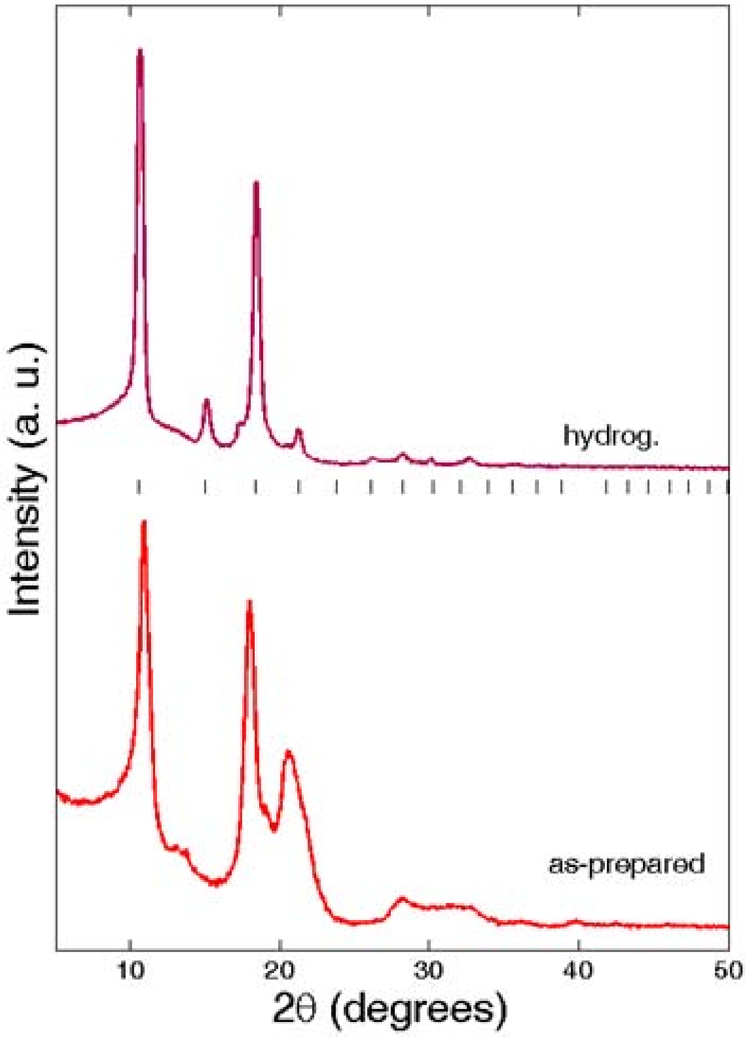

Figure 4.5: X-ray diffraction profiles of $Li_6Pd_{0.07}C_{60}$ collected on the pristine sample (red line) and on the sample after hydrogenation (purple line). The black ticks mark the reflection positions of the hydrofullerene $C_{60}H_{36}$.

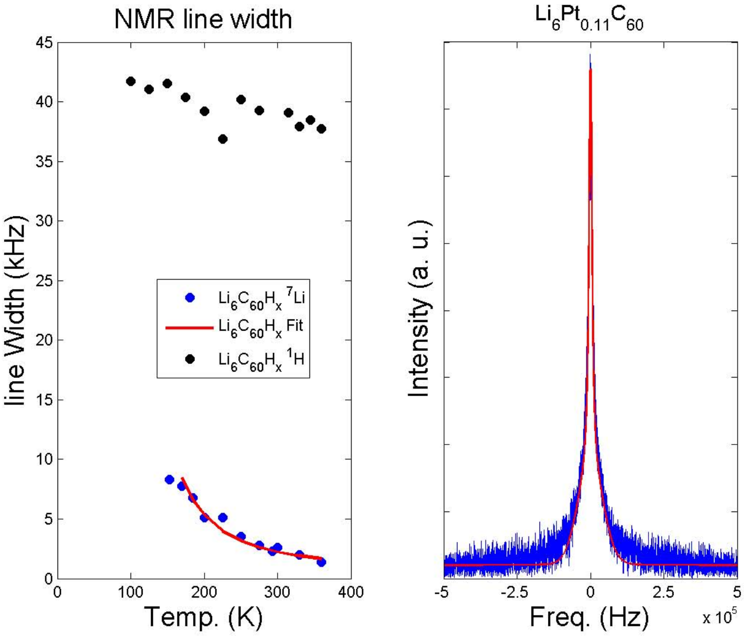

Figure 4.6: Nuclear Magnetic Resonance line bandwidth results for ^{7}Li and ^{1}H nuclei on hydrogenated Li_6C_{60} (left panel) and room temperature NMR signal (blue color) and fitting (red color) of $Li_6Pt_{0.11}C_{60}$ (right panel).

After the hydrogen treatment, the crystalline structure changes and the peaks can be indexed with a *bcc* cell with a=11.81(6)$\dot{A}$, similarly to what observed in $Li_6Pt_{0.11}C_{60}H_y$. In this case, no spurious phases arising from metal hydrides segregation (LiH or PdH_x) or carbonaceous phases different from the hydrofullerene are clearly evident in the diffraction pattern, indicating that the hydrogenation process of this sample is homogeneous.

In order to clarify over the formation of lithium hydride in these Li intercalated fullerides we performed Nuclear Magnetic Resonance on $Li_6C_{60}H_{40}$. Figure 4.6 (left panel) reports the signal bandwidth of hydrogenated Li_6C_{60} for both ^{7}Li and ^{1}H nuclei.

Since the NMR bandwidth depends on the dipolar interaction (in case of diamagnetic compounds where the hyperfine coupling is absent) it is strongly dependent on the spin-spin interaction and therefore it is sensitive to different chemical compounds. A direct information on lithium environment in Li_6C_{60} can be obtained when full width at half maximum (FWHM) temperature dependence is considered. ^{7}Li resonance possess a lorentzian line whose width exponentially increases upon temperature reduction, in agreement with a motional narrowed environment which determines a dynamical averaging of the dipolar interaction sensed by Li ions. ^{1}H signal has a gaussian lineshape and is slightly linearly reduced decreasing T. This states that H atoms are bound in a static condition, and therefore they are not providing the dynamical behaviour involving ^{7}Li. The picture that is depicted by NMR experiments can be described with static hydrofullerene molecules intercalated with Li ions which travel between different positions in unoccupied internal voids. This motion, which causes a dynamical homonuclear (with other Li atoms) and etheronuclear (with H atoms) dipolar interaction, is promoted by temperature. The presence of unbound Li is a clear indication of LiH absence in lithium fullerides after hydrogenation. When NMR study is extended to $Li_6Pt_{0.11}C_{60}$ it shows that lithium hydride is absent in transition metal doped compounds also. ^{7}Li NMR (right panel) room temperature signal reveals lithium is in a diamagnetic environment, motivated by few herz of chemical shift with respect to LiCl-solution reference signal. This resonance is clearly the convolution of a lorentzian sharp peak and a gaussian broader decay and can therefore be attributed to the contemporary presence of lithium subject to a dynamic motion and to a static one. FWHM is around 20 kHz, resulting from the sum of the two features. This signal is clearly sharper than the lithium resonance line in pure Lithium hydride (30 kHz broad, results not shown) thus excluding the presence of LiH in $Li_6Pt_{0.11}C_{60}$ after the hydrogenation step.

Scanning electron microscopy was applied in order to provide investigation of the samples under the morphological point of view. Figures 4.7 report the secondary electrons SEM pictures of the samples both as prepared and after hydrogenation at different magnifications.

As-prepared $Li_6Pt_{0.11}C_{60}$ and $Li_6Pd_{0.07}C_{60}$ (a,c) powders are composed by aggregates of very different size distribution, in the range 560 μm, made in turn of particles even smaller than 1 μm. After hydrogenation (b,d), the size of the aggregates decreases considerably, and the powder is more fragile and fine-grained. The crystallite size remains the same as in the pristine powders. The same has been observed happening in Li_6C_{60} (results not shown). Panels a and c of Figure 4.8 report the backscattered electron images which show that the platinum and palladium metals are present as 1μm or submicron granules homogenously dispersed inside the Li-C matrix in pristine samples. The dispersion is retained also after hydrogenation (panels b,d in Figure 4.8).

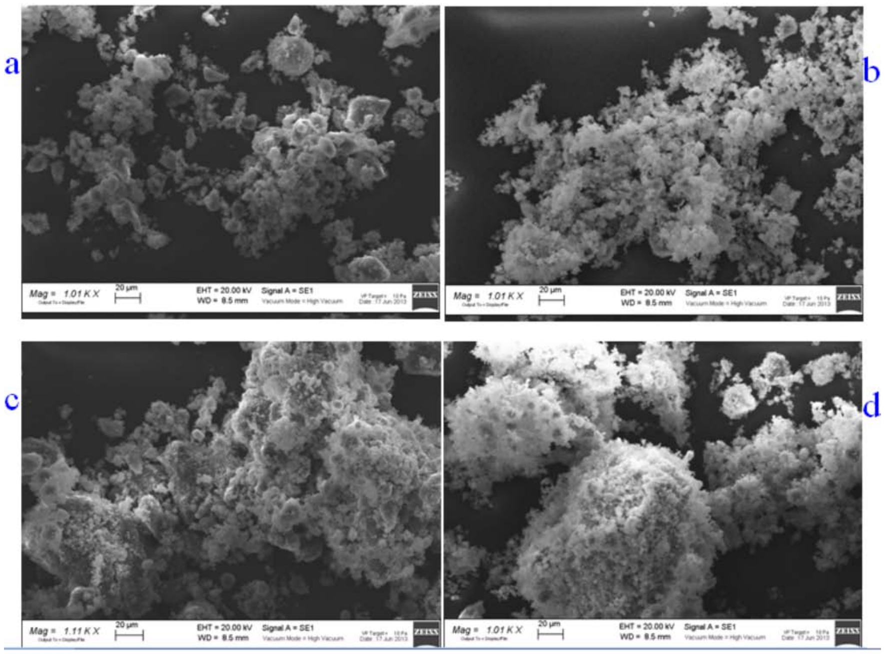

Figure 4.7: SEM secondary electrons images of pristine and hydrogenated $Li_6Pt_{0.11}C_{60}$ (a,b) and $Li_6Pd_{0.07}C_{60}$ (c,d).

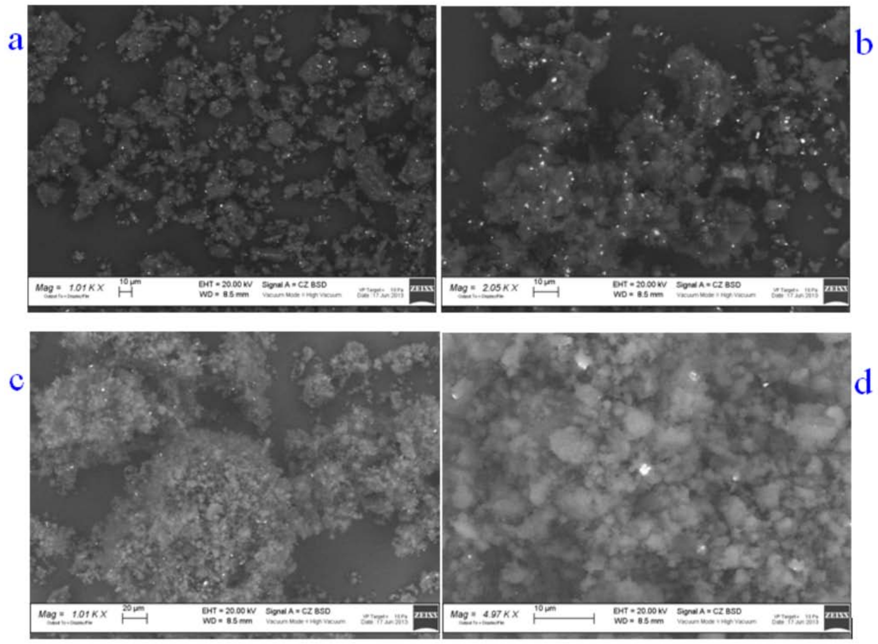

Figure 4.8: SEM backscattered electron images of $Li_6Pt_{0.11}C_{60}$ and $Li_6Pd_{0.07}C_{60}$ in pristine conditions (a,c respectively) and after hydrogenation (b,d).

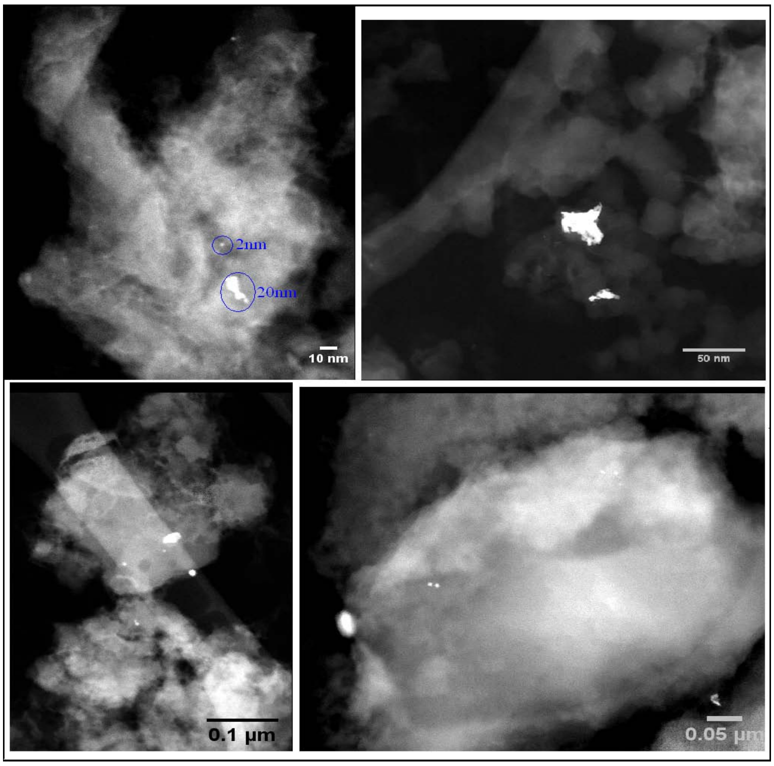

[h]

Figure 4.9: HAADF-STEM images collection at various magnifications on different $Li_6Pt_{0.11}C_{60}$ positions. Pt clusters and particles appear bright in these images (dark field) due to sensitivity of the technique to the atomic number the component.

In order to study the presence of particles with dimensionalities lower than the scanning electron microscopy resolution, scanning transmission electron microscopy (STEM) was applied on the $Li_6Pt_{0.11}C_{60}$ sample. Due to its contrast proportionality to the atomic number of the element in the sample Z^{α} (where $\alpha \sim 2$) STEM provides information on the presence of nanosized structures, thanks to its sub-nanometer resolution. Figure 4.9 reports selected images at various magnifications of the platinum decorated sample powder: they reveal that the fulleride matrix is indeed decorated by nanometer sized particles.

Fragments appear to be distributed over the range from 2 nm up to hundreds of nanometers, therefore the ball milling condition produces a platinum segregation on a broad size distribution of particles which range from the nanometer scale up to the micron-sized aggregates.

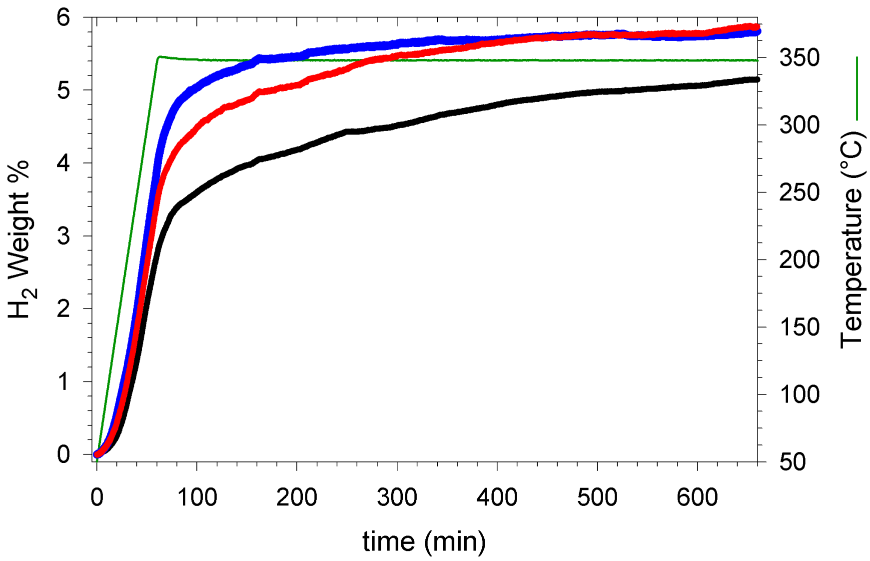

Figure 4.10: Kinetic absorption curves for the Li_6C_{60} sample (black line), for the Pt decorated sample (red line) and for the Pd containing one (blue line). The temperature ramp profile is also reported (green thin line).

4.2.2 Hydrogen storage properties

Figure 4.10 reports the kinetic curves of the pure Li_6C_{60} compound (black line) compared with the best results among Pt and Pd doped samples (red and blue line, respectively).

As evident, both transition metal decorated samples absorb more than 5 wt% of hydrogen in the selected experimental conditions. The doped samples however reach a hydrogen charge value of 3 wt% and 4 wt% at 295 °C and 345 °C respectively, while for the pure sample the same hydrogen content is reached at 350 °C, during the isothermal stage. Moreover, the final gravimetric capacity is higher for the transition metal-doped samples with respect to the pure one (about 5.9 wt% vs 5.1 wt%). Such an increase in the final uptake values with respect to Li_6C_{60} reflects an average stoichiometric hydrogen values $Li_6Pt_{0.11}C_{60}$-H_{47} and $Li_6Pd_{0.07}C_{60}$-H_{46} while in the pristine sample Li_6C_{60}-H_{40} is achieved. The kinetic properties of lithium intercalated fullerides are modified as well. During the heating ramp the sorption rate is approximately $4.30 \cdot 10^{-2}$ wt%/min for the pure Li_6C_{60} compound, $5.55 \cdot 10^{-2}$ wt%/min for the Pt sample and up to $6.77 \cdot 10^{-2}$ wt%/min for the Pd containing one. By the coupled manometricDSC measurements (see Fig. 4.11), it is possible to conclude that the onset temperature for dehydrogenation decreases from 306 °C for the pure compound to 301 °C for the Pd containing sample down to 292 °C for the Pt one. On the contrary, the related dehydrogenation enthalpy values seems to increase a little, from 63 kJ/mol H_2 for the pure sample to 66 kJ/mol for the Pd one.

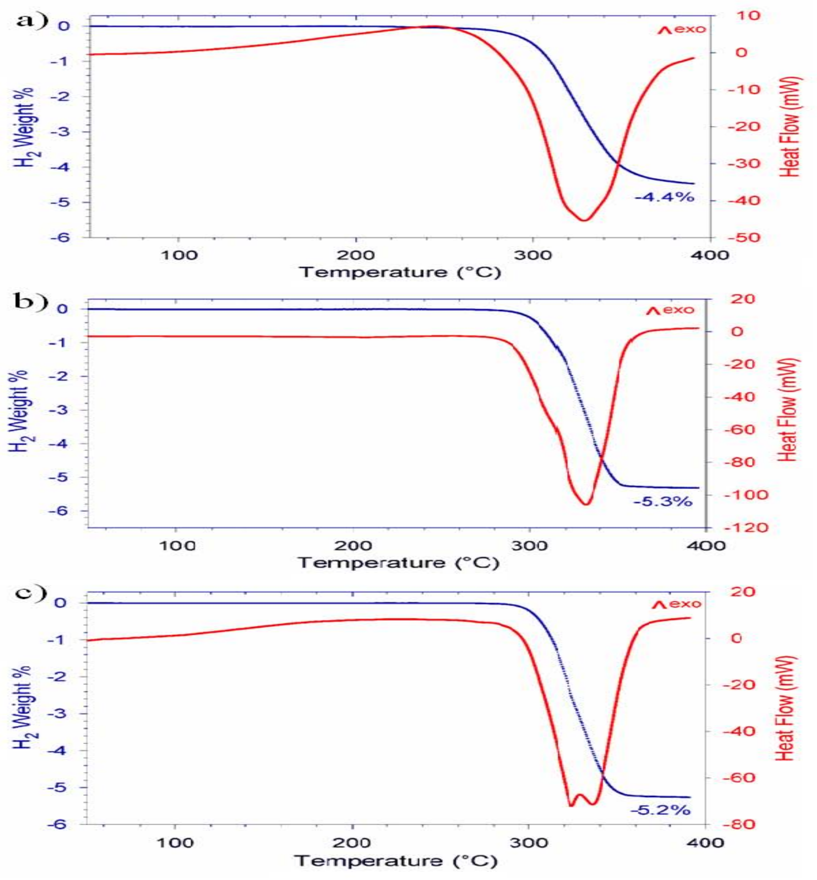

Figure 4.11: Coupled manometric-calorimetric desorption profiles for the bare Li_6C_{60} (a) and the doped samples $Li_6Pt_{0.11}C_{60}$ (b) and $Li_6Pd_{0.07}C_{60}$ (c).

When this analysis is extended to the different transition metal stoichiometries results shown in Fig. 4.12 are obtained.

In the platinum decorated system it is clearly possible to notice the existence of a stoichiometry range in which final uptake absorption values are enhanced with respect to pure Li_6C_{60} (5.0 wt%, (57, 121)). As a matter of fact, for Pt_x stoichiometries exceeding x=0.11 the amount of absorbed hydrogen is lowered and sets below the undoped

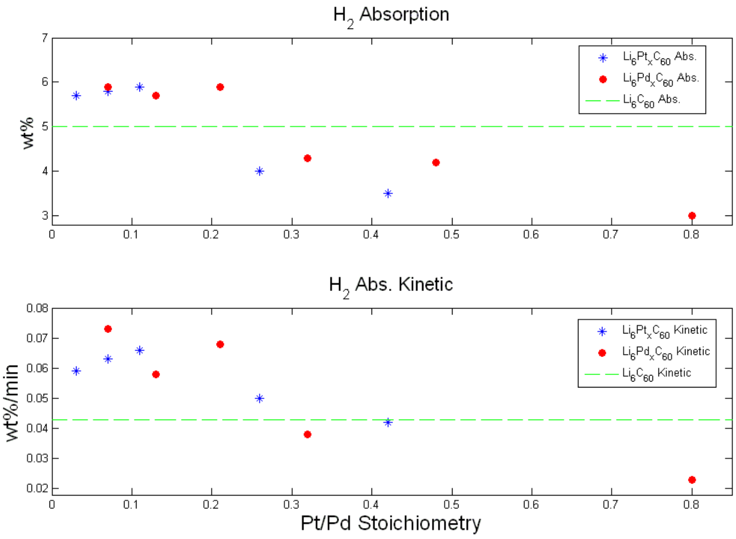

Figure 4.12: Final uptake (upper graph) and absorption kinetic values (lower graph) against stoichiometry of the transition metal.

sample. In palladium case, an improvement with respect to Li_6C_{60} is effective for the low transition metal stoichiometry values: when x is lower than 0.21 in $Li_6Pd_xC_{60}$ a final uptake amount of 5.8 wt% H_2 is obtained and, as happens in platinum case, this value falls below pure lithium intercalated fulleride for higher x values (x up to 0.8). It is worth noting that the maximum uptake decreases with the increase of the transition metal content for the stoichiometric values exceeding 0.11 and 0.21 respectively. Concerning the absorption rate during the heating step (see Fig. 4.12, lower panel), in the Pt series it increases with the transition metal stoichiometry (from $5.9{\cdot}10^{-2}$ wt%/min up to $6.6{\cdot}10^{-2}$ wt%/min) up to Pt content x=0.11, and then decreases (down to $4.2{\cdot}10^{-2}$ wt%/min for the Pt richest sample). The first three samples reach 5 wt% H_2 content after 200 min and their highest maximum content after about 400 min. The kinetic of the samples is better than for the pristine Li_6C_{60} powders with the exception of the Pt richest one. In the Pd series the best performance during heating are for the sample with the lowest transition metal content ($7.3{\cdot}10^{-2}$ wt%/min), followed by the ones with Pd stoichiometry y=0.21 ($6.8{\cdot}10^{-2}$ wt%/min) and y=0.13 ($5.8{\cdot}10^{-2}$ wt%/min). The measured rates are all higher than the bare Li_6C_{60} compound ($4.3{\cdot}10^{-2}$ wt%/min). On the contrary, for the samples with higher Pd content, the rate is lower and decreases by increasing the metal content (from $3.8{\cdot}10^{-2}$ wt%/min for y=0.32 to $2.3{\cdot}10^{-2}$ wt%/min for y=0.8), testifying that also for the kinetics too high transition metal contents worst the performance. Interestingly, the sample with y=0.21 shows the best kinetics during the isothermal stage, reaching a H_2 content of 5.5 wt% after 140 min at 350 °C and 5.9 wt% (its maximum gravimetric capacity) after 240 min. The other samples with lower Pd contents reach 5.5 wt% after 205 (y=0.069) and 250 min (y=0.013) and their maximum hydrogen content after 400 and 560 min respectively. The best kinetic results are found on the samples with the highest gravimetric capacities, as for the Pt family. By comparing the performance of the two families of compound, it can be noticed that the Pd containing samples are a little bit faster in absorbing hydrogen than the Pt ones. For all the samples, the absorption of small amount of H_2 starts already at temperatures as low as 70 °C, with the kinetics improving with the increase of temperature.

Concerning desorption, a systematic calorimetric exploration of these compounds reveals similarities in the desorption onset temperature for both series of samples (A selection of calorimetric profiles is shown in figure 4.13). With the addition of different platinum amounts the desorption onset is localized at 298 ($Pt_{0.26}$), 309 ($Pt_{0.07}$ and $Pt_{0.42}$), 300 ($Pt_{0.03}$) and 292 °C ($Pt_{0.11}$). In palladium compounds the absorption onset is detected at 301 °C (in $Pd_{0.07}$, $Pd_{0.13}$ and $Pd_{0.8}$) or at 294 °C ($Pd_{0.21}$).

Desorption thermal exchanges in calorimetric measurements are found as single peaks around 325 °C ($Pt_{0.03}$ and $Pt_{0.11}$), around 334 °C ($Pt_{0.26}$) or as double features around 327 and 337 °C (in $Pt_{0.07}$ and $Pt_{0.42}$). In case of palladium addition a double shaped calorimetric profile is more common with peaks localized around 325 and 335 °C, as found in $Pd_{0.07}$, $Pd_{0.13}$, $Pd_{0.21}$ and $Pd_{0.8}$ (even if some smaller features can be seen in the last two compounds at 345 °C). De-hydrogenation enthalpies set in the range 55-66 kJ/mol. In the platinum family 55 kJ/mol are obtained for Pt = 0.03; 54.67 kJ/mol for Pt = 0.07; 62.96 kJ/mol, 61.10 kJ/mol and 60.37 kJ/mol for Pt = 0.11, 0.26 and 0.42, respectively. Although a general trend may be detected since lower enthalpies are found with the addition of the lowest Pt stoichiometries, this causes a very limited variation in the process energy and is moreover not confirmed by the palladium series. In $Li_6Pd_yC_{60}$ a rather different phenomenology is found; the de-hydrogenation enthalpy is 66 kJ/mol for $y = 0.07$; 64.59 kJ/mol for $y = 0.13$ while it is 57.19 kJ/mol for $y = 0.8$. Intermediate palladium amount (y = 0.21) yield an enthalpy of 51.54 kJ/mol but the absorption process is still in progress at the upper investigated temperatures (380 °C).

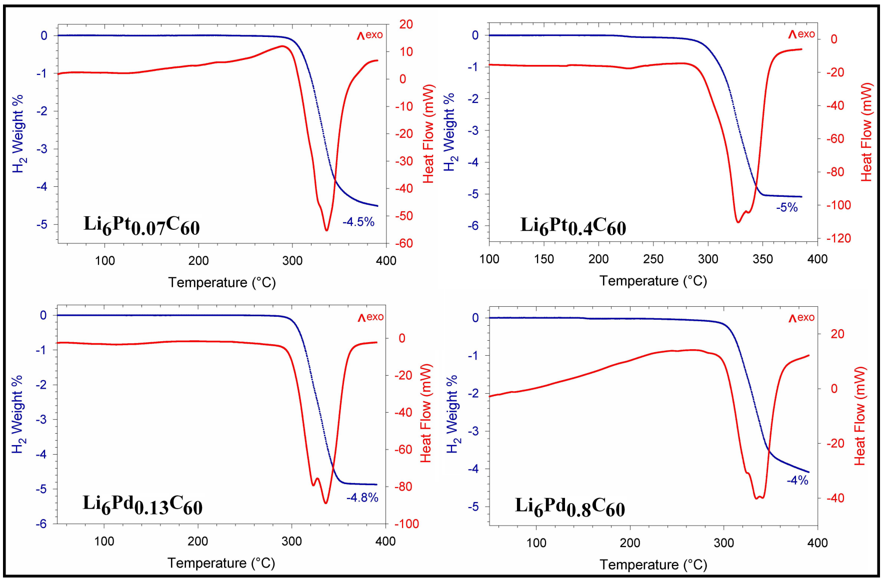

Figure 4.13: Selected images of coupled manometric-calorimetric desorption profiles representing Pt and Pd stoichiometric extremes.

Some small differences are found in sorption onsets and calorimetric maxima. However absorption temperatures are localized in a range of 20 °C and the appearance of two calorimetric peaks can be attributed to sample inhomogeneities (122). Furthermore reaction enthalpies are localized between 55 and 66 kJ/mol. Considering pure Li_6C_{60} de-hydrogenation enthalpy is 63 kJ/mol, we can conclude the same process drives H_2 desorption in pure and doped sanples. This single mechanism is to be attributed to the breaking of C-H bond in hydrofullerene molecules whose presence had previously been shown by XRD measurements for both lithium intercalated (57) and for transition metal-lithium fullerides (123). The insertion of Pt/Pd particles introduces a slight reduction of the reaction enthalpy in some stoichiometries only: a minor effect may be present in these compounds but the overall phenomenology seems to be a contribution in the absorption process only. In the TM intercalated systems we think that both alkali mediated and TM mediated dissociation mechanisms are effective, thus higher final uptake and faster kinetics are recorded; during the desorption step transition metal particles are instead not active in the destabilization of C-H bonding and therefore the reaction enthalpies result similar. Intercalated alkali clusters only, are effective in promoting $C_{60}H_n$ molecule collapse: this explains why hydrogenation enthalpies of transition-metal lithium fullerides resemble the values known for intermetallic compound Mg_2NiH_4 (124) and pure $LiBH_4$ (125) rather than the higher values which are expected for hydrogenated carbon species (126).

4.2.3 Comprehension and Interpretation of Absorption properties

Carbon is particularly suitable as can be easily hydrogenated but nonetheless the C-H binding energy is quite larger than what is required for practical applications. The C_{60} molecule can be hydrogenated to more than $C_{60}H_{40}$ (127) without displaying collapsing or fragmentation (128). Moreover ab initio calculations suggest C_{60}-H_x (x=36, 48) as the most stable structures (129) among highly symmetric $C_{60}H_{12*n}$. Such high values are probably met both in lithium intercalated and in transition metal decorated fullerides. On the other side the high binding energy issue has been partially reduced (57, 58) by the intercalation of light, partially ionized, alkali clusters (Li, Na) in the fullerene lattice which dramatically decreases the C-H binding energy, probably thanks to the highly charged state of C_{60}. Although the synthesis of $Li_6TM_xC_{60}$ (TM= Pt, Pd) started from a homogeneous Li-TM alloy, the high cohesion energy of TM induced its segregation into dispersed particles which are indeed still active in enhancing the dissociation process. In order to demonstrate that this enhancement is ascribed to the TM catalytic activity and not to the simple hydrogenation of the TM we should exclude the formation of TM hydride in our hydrogenated samples. The platinum hydride to be formed needs much higher pressure (27 GPa) than the one applied during manometric measurements (130). Also the presence of a ternary hydrides may be ruled out in $Li_6Pt_{0.11}C_{60}$ since no diffraction peaks which belongs to any of their hexagonal phases may be detected in patterns presented in Figure 4.4 (131, 132, 133, 134). A different situation is met in case of palladium. The formation of palladium hydride (135) which do not need extreme pressure conditions like Pt, may be as well obtained upon hydrogenation (different hydrogen concentrations x=0.65 (136), x=0.74 (137) are reported in the literature). However no signature from x-ray is given confirming the presence of such a phase (see Figure 4.5). Furthermore no diffraction due to palladium related compounds can be found in the hydrogen treated $Li_6Pd_{0.07}C_{60}$-H_{40}. On the other hand we recently demonstrated (58) that the hydrogenation of these fullerides takes place through the formation of an intermediate alkali metal hydride phase which is shown by X-ray diffraction in the hydrogen loaded material, when the alkali stoichiometry is larger than 8-10. Probably, in these cases the high internal chemical pressure developed

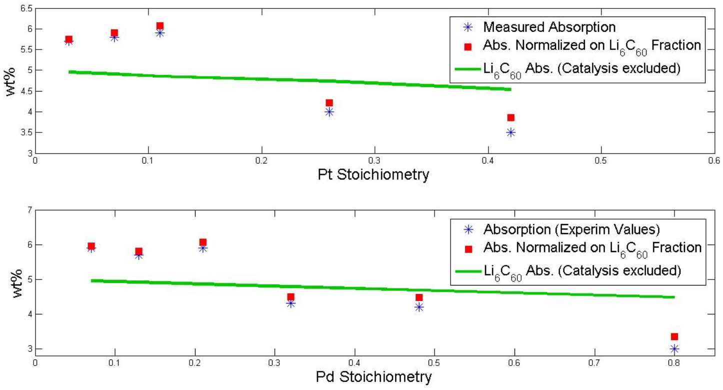

Figure 4.14: Absorption values obtained from manometric measurements (blue asterisks), final uptake values normalized on the absorbent Li_6C_{60} fraction (red squares) and calculated absorption values of the fulleride component only, after exclusion of the transition metal fraction (green line).

during hydrogenation induces the segregation of alkali hydrides particles in the lattice. This effect is absent at lower stoichiometries (like in our case) in which no segregation is observed. In order to summarize we believe in the TM intercalated systems two mechanisms are effective: alkali mediated and TM mediated dissociation. Since the reversible hydrogenation of the C_{60}^{n-} results to be much more favored with respect to the neutral molecule, we think that a further improvement in the H_2 dissociation rate would result in a further overall increase of the reversible storage capabilities of these systems.

4.2.4 Understanding the stoichiometry-dependent Efficiency

The reduction of the final hydrogen uptake amount upon increasing of the platinum or palladium stoichiometry may be a consequence of the increase in the quantity of the transition metal. This can be ruled out considering data reported in Figure 4.14, which shows the measured final uptake absorption (blue asterisks), the absorption normalized over the fraction of Li_6C_{60} (red squares) and the absorption forecast (green line) for the fulleride amount in the corresponding stoichiometry.

These last values report calculations of the absorption of the fraction of pure Li_6C_{60} and were obtained through the subtraction of the transition metal weight and the exclusion of its catalysis. The pure lithium intercalated fulleride absorption was assumed

5 wt% H_2, as shown in literature and in Figure 4.12, and this was reduced by the relative percentage of the fulleride in the material. This calculation allows to compare the dependence of the absorption on the fulleride fraction only, thus excluding its reduction upon increasing platinum stoichiometry and account the decrease of the final hydrogen uptake amount in terms of lithium fulleride absorption efficiency. Even if a small decrease of storage property can be detected upon increasing the transition metal amount for both platinum and palladium, this is clearly not on the same order of magnitude of the measured absorption lowering. When the final uptake amount is normalized over the absorbent material a net increase with respect to the measured values may be detected. This increase, recorded on the enhancement of the platinum stoichiometry, shows that the absorption efficiency of these materials falls below 5 wt% H_2 measured in pure Li_6C_{60} in a too pronounced way to be explained by the abolition of Pt catalysis only. Considering the difference between normalized values at high Pt stoichiometries, the lower amount of absorbing fraction is therefore surely limiting the storage on the higher Pt and Pd stoichiometries, but a detrimental activity worsening the active absorbing fraction efficiency and based on the transition metal presence has to be introduced to properly describe differences in the experimental and expected absorbed H_2 weight.

The considerable difference in the absorption values upon increasing Pt and Pd stoichiometries may be motivated by differences in the size of transition metal particles. The formation of particles with bigger dimensionalities is indeed expected to lower the surface/volume ratio thus hindering the hydrogen dissociation accomplished on the particle surfaces. In order to investigate such a phenomenon we investigated $Li_6Pt_{0.42}C_{60}$ with High-Angle Annular Dark Field (HAADF) Scanning Transmission Electron Microscopy (STEM) and High Resolution Transmission Electron Microscopy (HRTEM): the former provided an overview of particle distribution in the samples, since its contrast is sensitive to the atomic number, the latter investigated morphology and structure of transition metal particles. It is worth mentioning here that this study and the one presented in the next paragraph focused on platinum samples because of their higher final uptake values. A collection of STEM images from various sample positions and at different magnifications is shown in Figure 4.15.

STEM show that in this sample a broad distribution of particle size is present: smallest clusters have 2 nm diameter while the biggest that were detected are local-

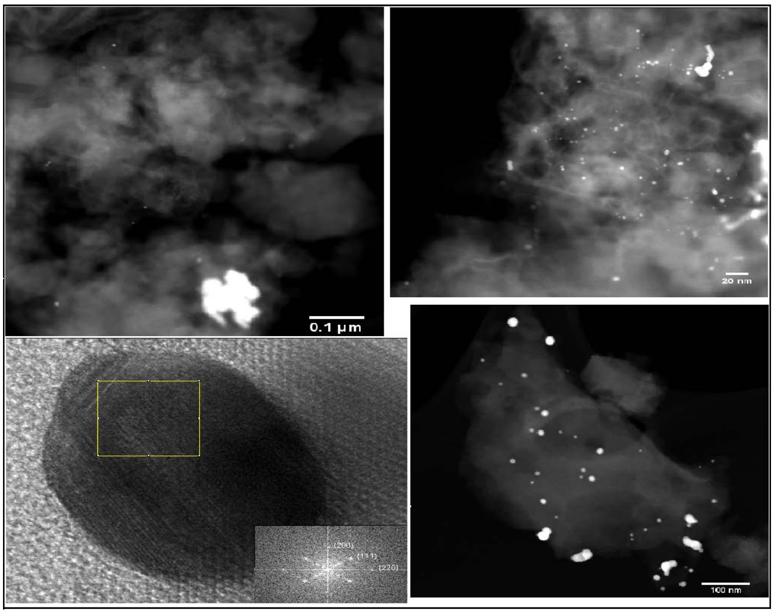

Figure 4.15: HAADF-STEM images at various magnification of $Li_6Pt_{0.42}C_{60}$. The Pt particles show up very bright in the image (dark field) due to the higher atomic number. Lower left panel include HRTEM image and FFT analysis from the square domain on a 25 nm particle, with sharp spots from an ordered cubic platinum structure.

ized around hundreds of nanometers as similarly shown for $Li_6Pt_{0.11}C_{60}$ in Figure 4.9. Micrometer sized particles, which are present in SEM study (see previous paragraph or (123)) are not observed in TEM but we suppose this is a consequence of powder dispersion in the solvent. HRTEM picture in Figure 4.15 and its fast Fourier transform (FFT) in the inset have atomic columns at positions compatible with cubic structure of Pt (space group 225, symmetry Fm3m) with the (200) reflection corresponding to 0.20 nm, (111) corresponding to 0.22 nm and (220) reflection corresponding to 1.38 nm plane distance in the real space. TEM description of $Li_6Pt_{0.11}C_{60}$ and $Li_6Pt_{0.42}C_{60}$ clearly shows that the distribution of particles which is obtained in these hybrid materials is the same and covers up three order of magnitude (from 2 nm to micron sized). The number of particles results increased in the compound with higher stoichiometry, this may therefore suggest an enhancement in the platinum surface available for H_2 dissociation catalysis; these results can therefore not motivate the massive difference in absorption results.

In order to understand if the addition of transition metal nanoparticles has influence on C_{60}^{n-}, Raman spectroscopy was applied on the $Li_6Pt_xC_{60}$ (x=0.11, 0.42). In the literature it is reported that the $A_g(2)$ Raman mode of C_{60} is very sensitive to polymerization and charge transfer (138). An empirical rule states it is shifted to lower wavenumbers by 6-7 cm^{-1} for every electron transferred to C_{60} (139, 140) and 5 cm^{-1} per polymer bond (141) due to the softening of the bond stretching modes as the electrons occupy the antibonding molecular orbitals. Figure 4.16 reports the position of $A_g(2)$ for the low and high Pt and Pd doping.

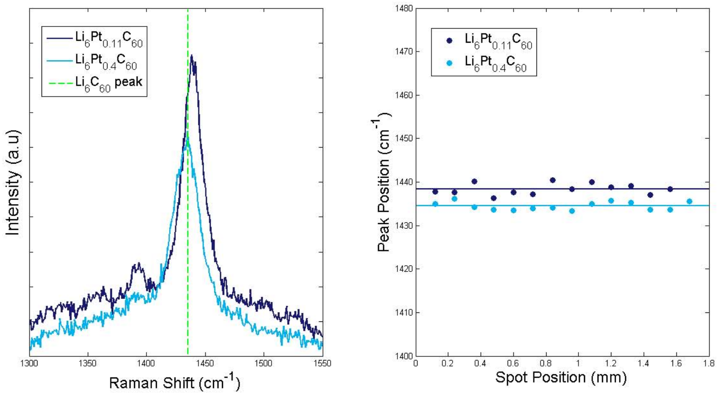

Figure 4.16: Raman spectra centered around the $A_g(2)$ mode for $Li_6Pt_{0.11}C_{60}$ and $Li_6Pt_{0.4}C_{60}$ (left side) and Raman peak energy measured on different positions of capillaries containing the same samples (right side). Peaks around 1380 cm^{-1} show fullerene molecule $H_g(7)$ vibrational mode.

$A_g(2)$ Raman mode is localized at 1438(1) cm^{-1} in $Li_6Pt_{0.11}C_{60}$ and at 1434(1) cm^{-1} in $Li_6Pt_{0.4}C_{60}$, corresponding to a charge transfer of 4.7 and 5.3 electrons for $Pt_{0.11}$ and $Pt_{0.4}$ respectively. A charge transfer of 5.2 electrons is detected in pure Li_6C_{60} (shown with green dashed line), in agreement with the value reported in literature (57). Raman spectra were collected in various positions (around 15 for each sample, each distant 120 μm) for each capillary containing the two compounds to exclude possible sample inhomogeneities. The right panel of Figure 4.16 describes the position of $A_g(2)$ peak over the sample and confirms the peaks shown in the left part reflect the overall behaviour of the compounds, even if small intrinsic differences, ascribable to samples inhomogeneities, are present.

$Pt_{0.11}$ stoichiometry triggers a reduction of half an electron (average value) of C_{60} charge with respect to the pure lithium fulleride, and the corresponding sample shows a net increase of H_2 absorption and kinetic. When increasing the amount of platinum to $Pt_{0.4}$ stoichiometry a charge similar to Li_6C_{60} is obtained and both uptake and kinetic result lower than the previous stoichiometry. Even if the net charge seems not to be correlated with the absorption (i.e. the same charge is found on Li_6C_{60} and $Na_{10}C_{60}$ while these two samples present rather different absorption properties), and it is not completely understood how the addition of transition metal particles may alter a bulk property of the material, we suggest this feature contribute to the worsening of absorption properties which we showed in figure 4.12, in a qualitatively similar way to the expected modification of the binding energy occurring on the charged molecule (33).

Indeed, the lithium stoichiometry study on pure fullerides (57) highlighted a linear relationship exists between the mole ratio C_{60}:Li and the number of hydrogen atoms per Li atom which determines a trend in the absorption efficiency. This behaviour has been attributed to the lithium effect in the formation of the active hydrogen storage material, but it has not been investigated whether this is due to lower element presence in intercalated clusters or to a different charge transfer on fullerenes.

It is possible to raise the hypothesis that the addition of a relatively small amount of transition metal provides a small charge variation which does not preclude the chemical absorption, further enhanced by the platinum driven catalysis, thus realizing the most suitable condition for uptake and kinetics. When the amount of metal is enriched the charge on the fullerene is increased, therefore probably lowering the system efficiency in a complex and not completely understood way.

Both the reduction of the active absorbing fraction 4.14 and the fullerene charge alteration 4.16 therefore contribute to and describe the hydrogen absorption decrease upon transition metal increase.

4.3 Exploration of transition metal addition to Li_6C_{60}

Transition metals different from either platinum or palladium may be used to prepare hybrid lithium intercalated fullerides, but often alloys can not be applied since many transition metals do not have solubility with lithium. This section details the structural results and the H_2 storage properties of TMs added fullerides using halogenides as described in the synthesis involving chlorides presented in Chapter 3.

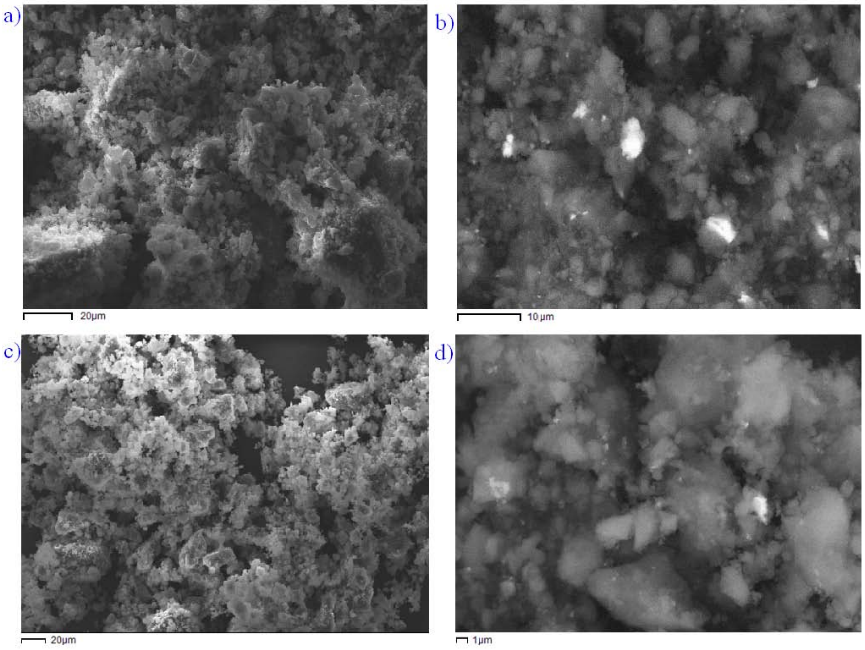

Figure 4.17: SEM secondary electrons (a, c) and backscattering images (b, d) of pristine (a, b) and hydrogenated (c, d) $Li_6Ni_{0.11}C_{60}$ at various magnifications.

4.3.1 Nickel addition from $NiCl_2$: structural results

Scanning electron microscopy and energy dispersive X-ray spectroscopy was applied on $Li_6Ni_{0.11}C_{60}$ to investigate powder composition and detect the presence or the decomposition of the small amounts of metal chloride. Figure 4.17, panels b, d and Table 4.2 show sample zones where the elemental analysis of pristine and hydrogen treated compounds was done.

	Pristine		Hydrogenated	
Element	Weight %	Atomic %	Weight %	Atomic %
C	70.6	86.68	93.53	95.79
O	5.68	5.24	4.87	3.75
Ni	12.89	5.36	0.91	0.32
Cl	10.83	2.72	0.69	0.14

Table 4.2: $Li_6Ni_{0.11}C_{60}$ sample composition estimated with SEM energy dispersive X-ray spectroscopy.

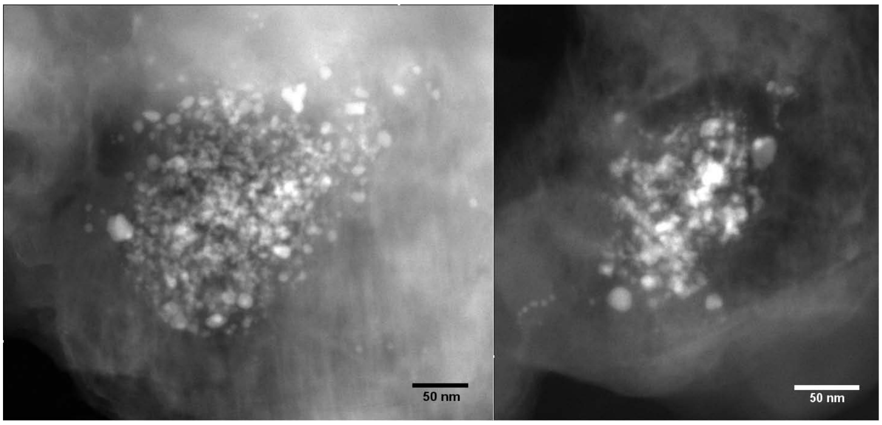

Figure 4.18: HAADF-STEM images of hydrogenated $Li_6Ni_{0.11}C_{60}$.

Brighter particles with grain-size lower than 4 μm are clearly detectable in Figure 4.17 (panel (b)). Energy dispersive spectroscopy detects these particles on both pristine and hydrogenated conditions, and the atomic concentration ratio of Ni and Cl is moreover identical to the precursor. It is unfortunately not possible to obtain reliable data on either carbon or oxygen relative concentration because of the glued-graphite support used during sample handling in SEM investigations. As-prepared $Li_6Ni_{0.11}C_{60}$ powders are composed by aggregates of different size distribution, up to around 50 μm, with lower particle size smaller than 1 μm. After hydrogenation (panels c,d in Figure 4.17), the size of the aggregates decreases to a finer grain size with the biggest particles approximatively 10 μm.

HAADF-STEM was applied to gather images concerning nano grain-sized objects and energy despersive study was repeated with the advantage of a smaller nominal probe size than in SEM. STEM pictures, reported in figure 4.18, describe the formation of particles approximatively localized between 3 and 30 nm, whose chemical composition shows a strong predominance of nickel with respect to Cl. When the intercalated fulleride matrix is analyzed the amount of chlorine strongly exceeds the nickel one, suggesting that Cl is engaged in LiCl formation. Clearly carbon signal is much stronger than the Ni and Cl ones due to the C_{60} compound, oxygen is instead present as a consequence of exposure to O_2 and moisture during sample preparation for STEM study.

After the hydrogenation nanoparticles are curiously often found in isolated regions, where they are found in groups. It might be suggested that the distribution which is shown in pictures 4.18 is achieved because $NiCl_2$, crystals, whose size is driven by high energy ball milling, are releasing Ni atoms during their thermal docomposition and provide limited areas where the development of the nucleation process proceeds. Although a small amount of transition metal chloride may not undergo decomposition during hydrogenation treatment the scenario which is suggested by energy dispersive micro analysis is the nickel release and Cl capture by lithium belonging to the fulleride matrix. Particles can be approximately detected in the range 3 to 50 nm.

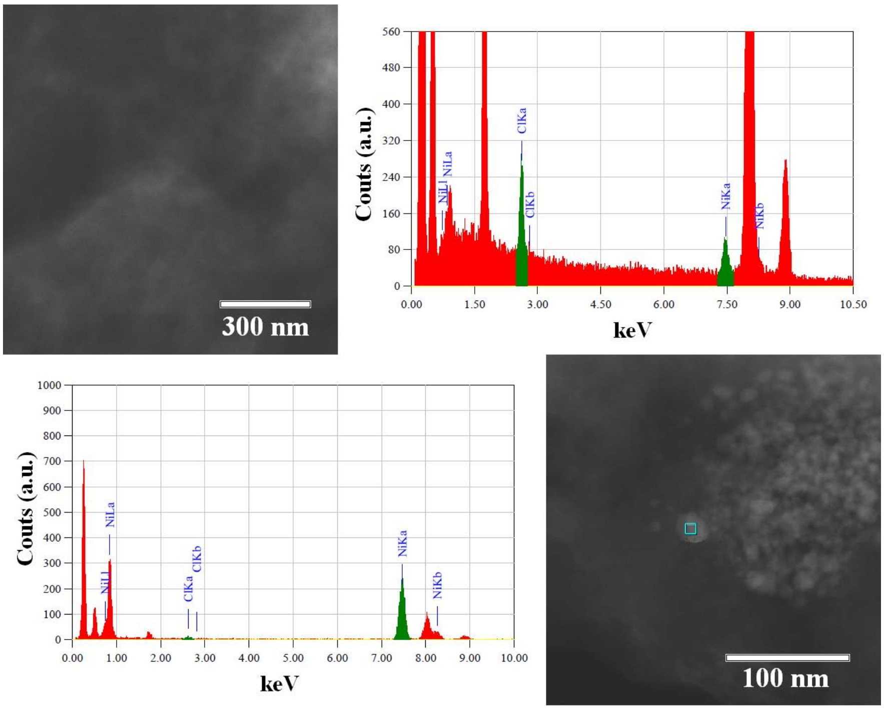

Figure 4.19: Energy dispersive X-rays spectroscopy elemental analysis of bulk material and particles and STEM images of investigated areas of hydrogenated $Li_6Ni_{0.11}C_{60}$. Light blue mark identifies EDX single particle detection.

On the bulk material the atomic percentage of Ni and Cl is 80.7 and 19.3, respectively. The single particle, instead, is mostly composed by nickel and only a small Cl fraction can be detected (Ni: 99.5, Cl: 0.5 atomic %). Stronger peaks belonging to carbon, oxygen and copper were detected also with energy dispersive spectroscopy (red colored in figure 4.19): the first is naturally present since the main component of our samples, the others belong to the copper grid which was used and to the oxidized

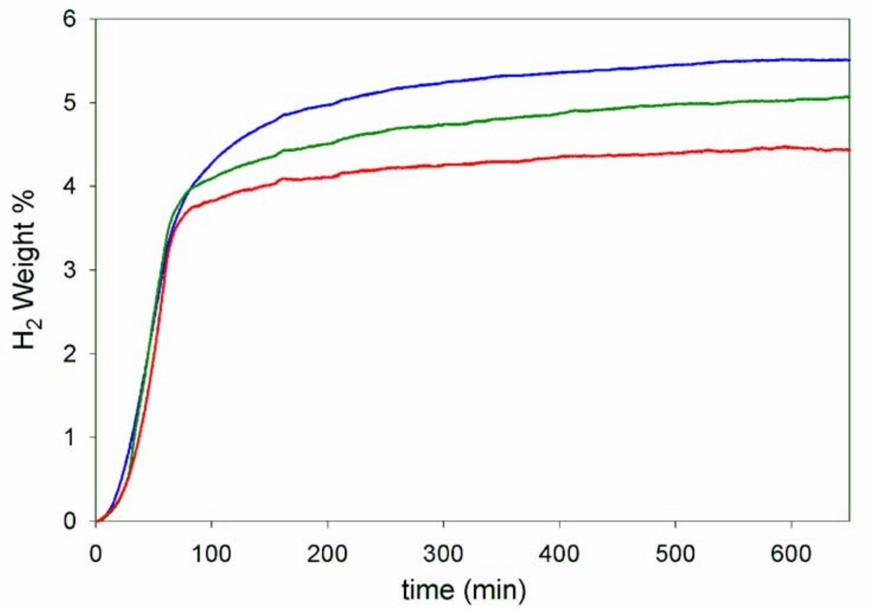

Figure 4.20: Kinetic absorption curves for $Li_6Ni_xC_{60}$ (x=0.11 in blue, 0.25 in red, 0.5 in green color.)

fulleride matrix which is achieved during air exposure of the samples (unavoidable to achieve the suspension). Such a topography can be motivated only with the decomposition of $NiCl_2$ precursor, which is introduced in the system with ball milling driven size. These crystals decompose at high temperatures during the H_2 treatment, providing a transition metal reservoir for Ni nucleation which is not distributing itself on the whole fulleride matrix but forming nanoparticles in the limited region previously occupied by the metal chloride only, and detected by HAADF-STEM 4.18.

4.3.2 H_2 storage in nickel decorated Li_6C_{60}

As in the case of platinum and palladium, nickel stoichiometry was explored in order to understand its contribution to the interaction with hydrogen and $Li_6Ni_xC_{60}$ (x=0.11, 0.25, 0.5) were obtained through the addition of nickel chloride to lithium intercalated fullerides. Manometric kinetic experiments were used to characterize these materials and are reported in Figure 4.20.

It is clearly evident from final absorption values that the addition of small amounts of transition metal (corresponding to its stoichiometry x=0.11) enhances the chemisorbed hydrogen amount to 5.5 wt% H_2 from 5 wt% which is found in bare Li_6C_{60}. A further increase of nickel quantity (stoichiometry x=0.25) lowers final absorption to 4.4 wt% while its doubling (x=0.5) reaches 5.1 wt% H_2. Concerning the absorption kinetics the three stoichiometries report similar values: $5.27{\cdot}10^{-2}$ wt%/min for $Li_6Ni_{0.11}C_{60}$, $5.11{\cdot}10^{-2}$ wt%/min for $Li_6Ni_{0.25}C_{60}$ and $5.54{\cdot}10^{-2}$ wt%/min for $Li_6Ni_{0.5}C_{60}$. DSC measurements, performed on the same samples, are reported in Figure 4.21. $Li_6Ni_{0.11}C_{60}$ presents the onset of an endothermal absorption at 304 °C and its profile is composed by two peaks at 326 and 338 °C. $Li_6Ni_{0.25}C_{60}$ has its onset at 301 °C and the same doubly shaped profile whose peaks are at 320 e 330 °C, as is shown in $Li_6Ni_{0.5}C_{60}$ also, where peaks are located at 318 e 331 °C, with the onset of the absorption at 298 °C.

$Li_6Ni_{0.11}C_{60}$ only presents a relatively large peak where the absorption is completed after 375 °C and the integration of the calorimetric profile allows determination of 62.39 kJ/mol binding energy. Higher Ni amounts seem to trigger the appearance of processes at higher temperatures which appear in DSC profiles (a raising heat absorption in $Li_6Ni_{0.25}C_{60}$ and a further feature around 365 °C $Li_6Ni_{0.5}C_{60}$ 4.21). Calorimetric measurements are broadened over a wider temperature range, probably extending over 400 °C, thus reflecting a slower process kinetic in the case of $Ni_{0.25}$ and $Ni_{0.5}$ stoichiometries. The desorption temperature seem to be stoichiometry dependent: on increasing Ni_x stoichiometry from $x = 0.11$ to $x = 0.25, 0.5$ the two absorption peaks are reduced from 326 to 320 °C and from 338 to 330 °C.

Even if a H_2 molecule spillover may be also introduced by transition metal chlorides (142), in our systems the salt is decomposed at surprisingly low temperatures. After metal release, chlorine is sequestered by lithium fulleride matrix as expected in the reaction 3.1, thus reducing the amount of intercalated lithium and explaining the loss of efficiency which is met upon increasing the nickel chloride amount. As in the case of platinum and palladium, manometric measurements seem to suggest the existence of a stoichiometry range which is introducing an effective surface catalysis. A nickel surface catalysis for H_2 dissociation has been intensively studied both theoretically (143, 144, 145) and experimentally (146, 147).

Calorimetric studies reveal a de-hydrogenation enthalpy of 62.39 kJ/mol for the lowest explored stoichiometry. Since no differences from pure Li_6C_{60} were seen in terms of enthalpies, the same desorption process is expected in the two compounds and nickel particles do not interefere with hydrofullerene collapse. When higher nickel

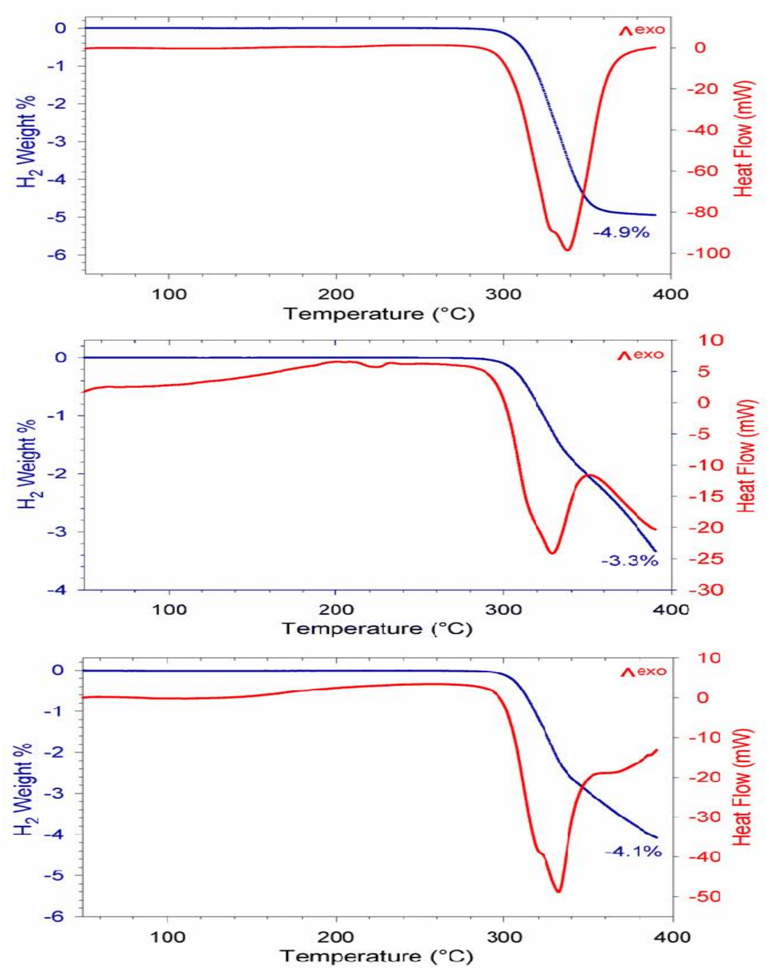

Figure 4.21: Differential scanning calorimetry analysis of $Li_6Ni_xC_{60}$ (x=0.11, 0.25, 0.5).

amounts are introduced in the system the amount of intercalated lithium is changed (and probably the charge beared by C_{60}^{n-} molecules also) and, thus, the efficiency of the absorbing fraction is modified and slower process kinetics, on both absorption and desorption events, are found. Since the addition of nickel chloride to lithium fullerides improved hydrogen absorption properties, some different transition metal chlorides were explored as described in the third chapter to extend this strategy (possibly) to the complete periodic table.

4.3.3 Absorption properties with Pd, Ti, Ce from chlorides

Palladium was first selected in order to compare results of the two synthetic strategies based on lithium alloys and metal chlorides. Titanium selection is motivated by its known catalytic effects towards hydrogen dissociation (43) and cerium was considered to extend this synthesis to rare earth elements. Manometric and calorimetric measurements of the decorated lithium fullerides are reported in Figures 4.22 4.23 4.24 for Pd, Ti, Ce decoration, respectively.

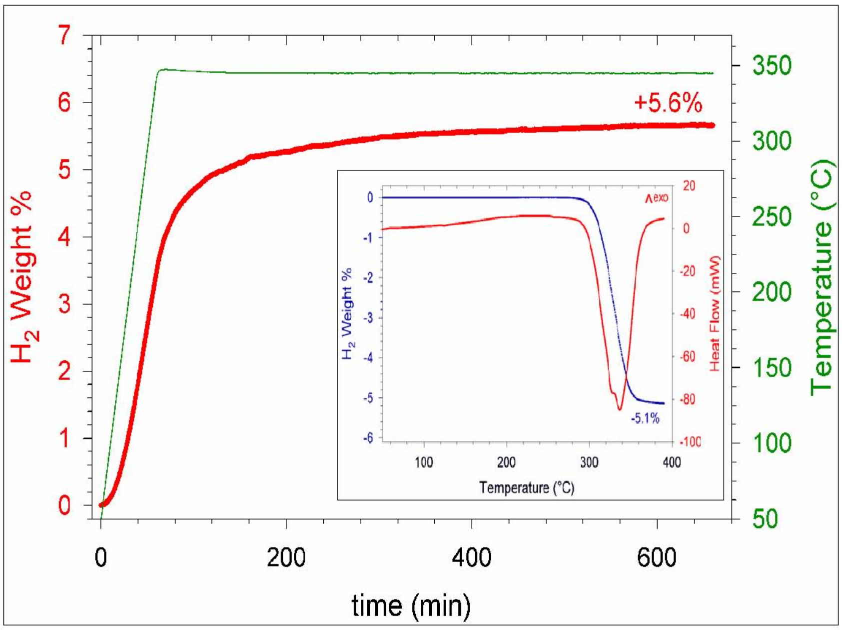

Figure 4.22: Absorption kinetic measurement of $Li_6Pd_{0.11}C_{60}$ obtained from metal chloride precursor. Inset: Calorimetric desorption profile. For undoped Li_6C_{60} measurement the reader should see Figure 4.10.

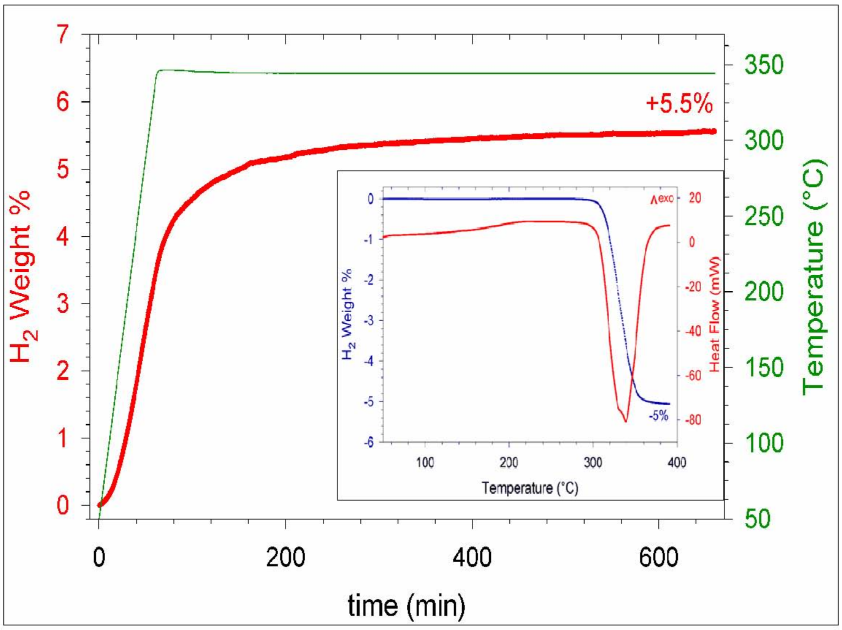

Figure 4.23: Absorption kinetic measurement of $Li_6Ti_{0.11}C_{60}$ obtained from metal chloride precursor. Inset: Calorimetric desorption profile.

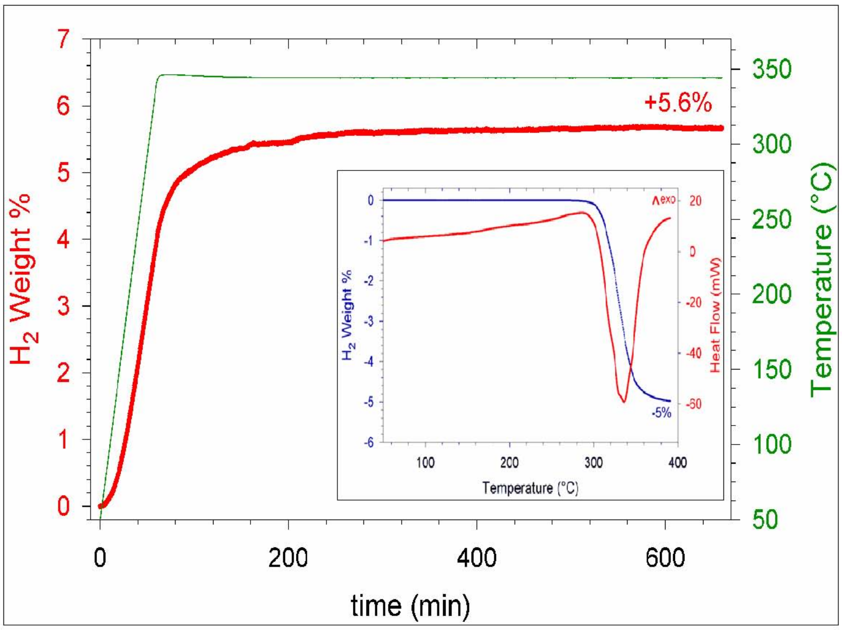

Figure 4.24: Absorption kinetic measurement of $Li_6Ce_{0.11}C_{60}$ obtained from metal chloride precursor. Inset: Calorimetric desorption profile.

Every sample absorbs more than 5 wt% of hydrogen in the selected experimental conditions. Palladium sample reaches a charge value of 5 wt% at 280 °C (it is useful to remind that undoped sample reaches this amount at 350 °C during the isothermal stage) and final gravimetric capacity of 5.6 wt%. In titanium decorated sample the threshold value of 5 wt% absorption is obtained at the end of the initial ramp at 288 °C and the final uptake amount is 5.5 wt%; after cerium decoration 5 wt% value is reached at 280 °C and a final uptake of 5.6 wt% is found. The kinetics of these samples are $5.85 \cdot 10^{-2}$ wt%/min for $Li_6Pd_{0.11}C_{60}$, $5.73 \cdot 10^{-2}$ wt%/min for $Li_6Ti_{0.11}C_{60}$ and $6.66 \cdot 10^{-2}$ wt%/min in case of cerium chloride addition. Calorimetric measurements are shown in Figures 4.22 4.23 4.24. Palladium sample presents the onset of absorption process at 304 °C and two clearly separated peaks at 329 and 337 °C. Concerning titanium sample the hydrogenation starts at 308 °C and two peaks can be recognized at 330 and 338.5 °C while Cerium containing sample possesses onset of hydrogenation at 308 °C and a clear double shaped absorption with maxima at 328 and 336 °C.

4.3.4 Transition Metals from chlorides: Discussion

The addition to lithium fulleride of metal chloride different from the nickel one, is able to provide as well a net increase in the final uptake value which is found in manometric measurements. Surprisingly, the absorption in these compounds sets on a 5.6 wt% H_2 average value, thus suggesting the similarity of different transition metals with respect to the interaction with hydrogen. Since ball milling reaction drives particles' size and the hydrogenation tests have been carried under the same conditions, different metal chloride particles are expected to be inserted in the system with similar grain size.

Even if we operated at temperatures which do not trigger the transition metal salt decomposition (as suggested by the literature on nickel (148) and SEM energy dispersive X-ray spectroscopy guaranteed the conservation of Ni/Cl atomic ratio, it has been demonstrated by STEM that chloride decomposition is achieved during the sample hydrogenation and therefore particles of transition metals are present during the heat treatment.

We can conclude that nanometer sized particles of different TMs (TM = Ni, Ti, Pd) trigger an increase in H_2 absorption beyond the properties of pure Li_6C_{60}, to be attributed to the catalysis towards H_2 dissociation driven by metal particles. A similar behaviour is reported upon the addition of a rare earth chloride (Ce).

On the stoichiometry $Li_6Me_{0.11}C_{60}$, every reported metal compound presents similar features in its calorimetric desorption profile. Their onset temperatures are 304 (Ni, Pd) and 308 °C (Ti, Ce). Differences in the activation energy for H_2 dissociation on different pure metal surfaces are predicted in theoretical publications (the dissociation energy is estimated 0.06 eV on Ni, 0.39 eV on Pd while negligible on Ti (101)). A minor effect due to metal insertion in fullerides may be therefore introduced to detail changes in the beginning of absorption but it is not possible to find a dramatic improvement since the onset of pure Li_6C_{60} is at 306 °C.

If we compare the results of palladium containing samples produced either with Li-Pd alloy or $PdCl_2$ addition we obtain a direct evaluation of the two different synthesis on the same metal ion in the same stoichiometry. This comparison shows a lower efficiency for the material prepared from chloride addition: this one achieves a final uptake result which is lower by 0.3 wt% H_2. Although the difference is very limited we suggest that it is motivated by slightly different amount of intercalated lithium or by variation in the charge beared by C_{60}^{n-} molecules, in agreement with the case of platinum and palladium decoration.

From the DSC study reported in Figures 4.21, 4.22, 4.23 and 4.24 it is evindent that two desorption processes are met when increasing temperature. These two calorimetric peaks are present in all samples prepared from metal chlorides and, as in the case of Pt/Pd their similarities (few degrees separates them in different compounds) can be attributed to sample inhomogeneities (122).

The related dehydrogenation enthalpy values are 62.80 kJ/mol for $Li_6Pd_{0.11}C_{60}$, 62.07 kJ/mol for $Li_6Ti_{0.11}C_{60}$ and 60.64 kJ/mol in the case of $Li_6Ce_{0.11}C_{60}$. If we compare these values with the enthalpy measured on $Li_6Ni_{0.11}C_{60}$, which is 62.39 kJ/mol and with 63 kJ/mol that are found for pure Li_6C_{60} it is possible to conclude that the catalysis which enhances absorption properties is not found during hydrogen desorption. This is probably happening as a consequence of the lack of a local presence of the transition metal nanostructures. The intercalated lithium clusters only are active during hydrofullerene dissociation and therefore dehydrogenation enthalpies result similar in pure and hybrid fulleride materials. In order to provide a more efficient de-hydrogenation catalysis a further improvement can be identified in the reduction of the nanoparticles volume distribution. Is such a development possible within the framework of solid state, solvent-free synthesis of lithium fulleride ionic compounds? A

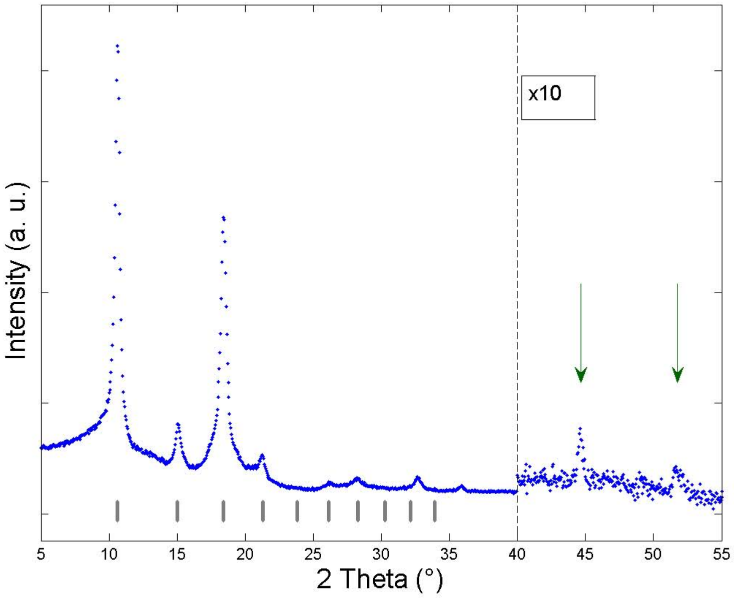

Figure 4.25: X-rays diffraction of hydrogenated $Li_6Ni_{0.11}C_{60}$ obtained from $(NBu_4)[Ni_6(CO)_{12}]$ clusters

suitable pathway involving metal clusters was developed in order to gain control over particle size.

4.4 Metal decoration from clusters: structural results

When nickel insertion is realized with metal carbonyl clusters a dispersion of Ni particles similar to the one found in case of chlorides is predicted since metal-carbonyl clusters are expected to release nickel over the lithium fulleride matrix during the hydrogenation thermal treatment upon heating up to 350 °C, as a consequence of their relatively low decomposition temperatures (around 150 °C (102)). X-rays diffraction and transmission electron microscopy indeed confirm this mechanism. XRD was performed on the sample enriched with $(NBu_4)[Ni_6(CO)_{12}]$ after its hydrogenation and is reported in Figure 4.25.

The main phase is constituted by a *bcc* crystalline structure (space group 204, a=11.80(4) $\dot{A}$) which is the arrangement that is commonly observed in the hydrofullerene $C_{60}H_{36}$ (116) and that has been detected after hydrogen loading of the platinum and palladium decorated compounds. Peaks of the *fcc* nickel metal (space group

225, simmetry Fm$\bar{3}m, a = 3.52\dot{A}$) can be observed in the higher 2Θ region ($10x$ magnification) and confirm the presence of nickel phase in the hydrogenated samples. This result has been confirmed by high angle anular dark field - scanning transmission electron microscopy study, which is reported in Figures 4.26 and 4.27 for both hydrogenated samples.

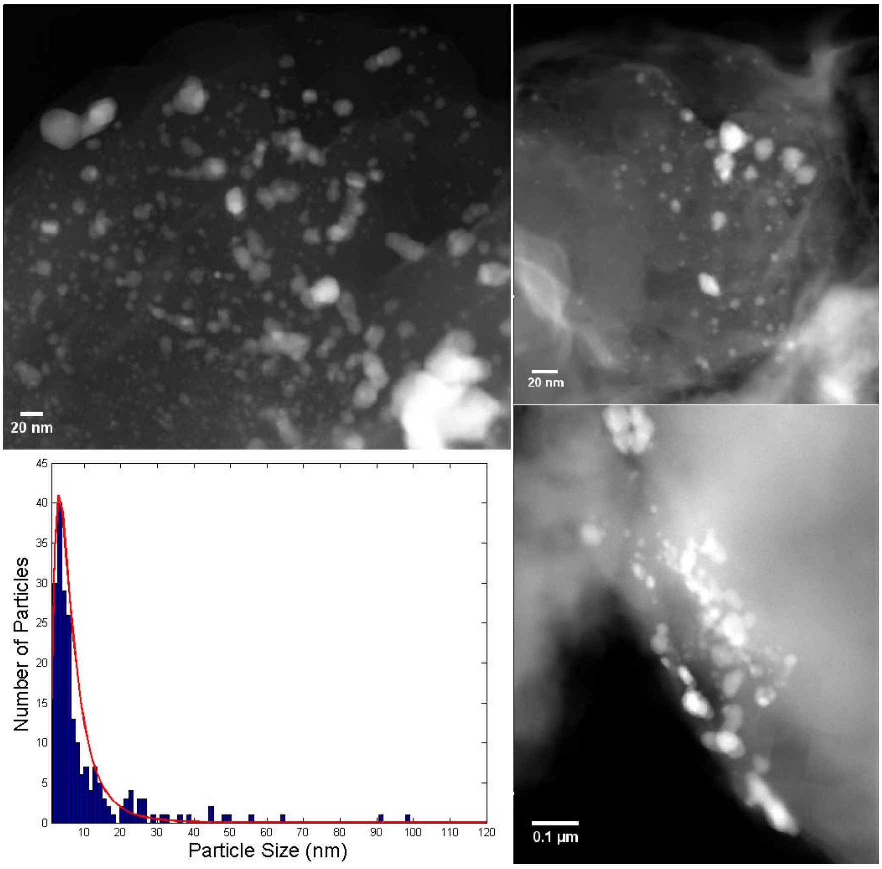

Figure 4.26: HAADF-STEM images of $Li_6Ni_{0.11}C_{60}$ obtained from (N-Bu_4)[$Ni_6(CO)_{12}$] clusters.

These images clearly show the presence of nanosized nickel particles since the contrast of this technique is sensitive to the atomic number of investigated sample. The hystograms in both Figures 4.26, 4.27 were obtained from the study of around 210 and 75 particles, for sample from Ni_6 and Ni_{12}, respectively. In both compounds particles sizes are mainly distributed in the relatively limited range 2-40 nm, apparently according to a logarithmic-normal distribution (149) which is commonly used to describe the formation of objects produced through fragmentation (150) and here show

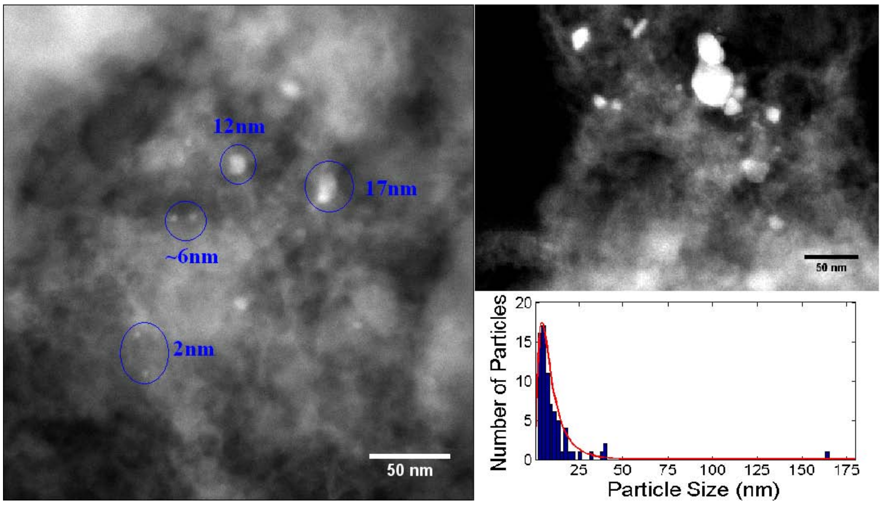

Figure 4.27: HAADF-STEM images of $Li_6Ni_{0.11}C_{60}$ obtained from $(NEt_4)_3[HNi_{12}(CO)_{21}]$ clusters.

mean values of 2.07 nm in Ni_6 and 1.79 nm in Ni_{12} sample. According to these results, thermal decomposition of carbonyl clusters releases nickel metal clusters which aggregate as a consequence of their relatively high reactivity thus creating, therefore, larger sized objects. The inhomogeneous size distribution is supposed to be dependent on the size of $(NBu_4)[Ni_6(CO)_{12}]$ and $(NEt_4)_3[HNi_{12}(CO)_{21}]$ powders which are obtained after grinding: these crystal are expected to act as Ni reservoir during their decomposition, providing the amount of metal available for Ni crystal growth dependent on the size of its precursor. The metal carbonyl cluster-based synthesis can therefore guarantee the production of nanometer sized particles with a relatively sharp distribution exploiting the application of a relatively clean, solid state technique.

4.4.1 Absorption properties with Ni clusters

Figure 4.28 reports both the kinetic curve and the calorimetric desorption profile of fullerides where nickel addition is obtained from transition metal-carbonyl clusters decoration with $(NEt_4)_3[HNi_{12}(CO)_{21}]$. Even if these must be considered preliminary results they provide a useful information on the future development of hybrid lithium fullerides.

Final absorption value, describing the chemisorbed hydrogen amount, results enhanced from pure Li_6C_{60} value to 5.5 wt% H_2, while its kinetic rate is similar to

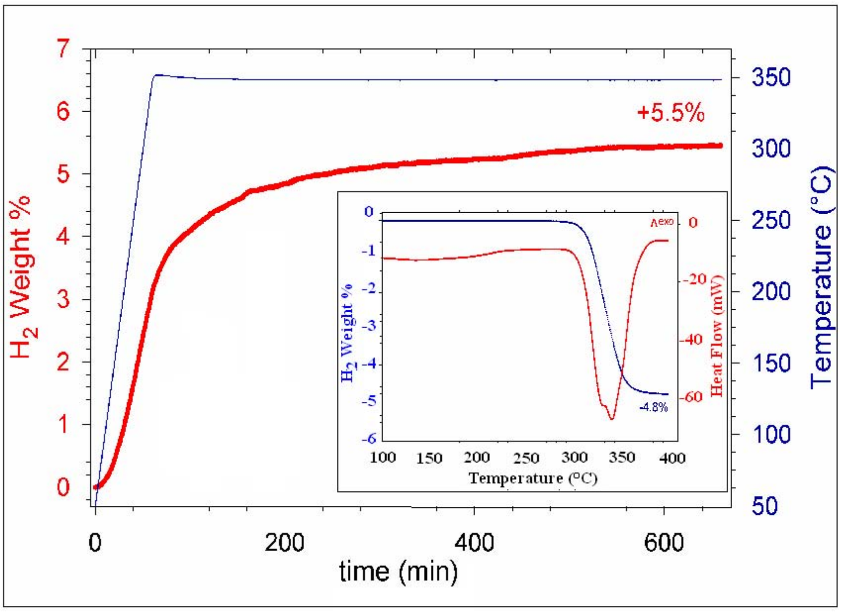

Figure 4.28: Kinetic absorption curves for $Li_6Ni_{0.11}C_{60}$ with nickel addition from $(NEt_4)_3[HNi_{12}(CO)_{21}]$ complex

platinum and nickel-doped lithium fullerides. It is reasonable to conclude, as shown in the previous cases, that nickel metal nanoparticles catalyze the molecular H_2 dissociation, thus enhancing the amount and the kinetic of absorption. During the desorption process the calorimetric profile reveals an onset around 306 °C and the superposition of two peaks at 328 and 337 °C, in good agreement with the sample where the transition metal addition is obtained from nickel chloride in the same stoichiometry. The related de-hydrogenation enthalpy is 57.3 kJ/mol, to be compared with 63 kJ/mol process in pure compound and 62.39 kJ/mol in $Li_6Ni_{0.11}C_{60}$ from $NiCl_2$. Even if this is a preliminary result, further studies are in progress and we do not detect a dramatic improvement with respect to pure and transition metal doped samples, this value may be considered a decrement of the process enthalpy which is achieved after particle size reduction. In this case the catalysis of nanometer sized particles would provide evidence on the destabilization of the desorption process therefore reducing the energy required for H_2 release from lithium intercalated fullerides. If this result will be confirmed, similar enthalpy values which were found in the lowest platinum stoichiometries might be explained as a consequence of transition metal particle size. Furthermore the route to possible future improvements of these materials could be easily identified in the pursuit of subnanometer sized transition metal decoration.

5

Conclusions

This thesis work moved from the many theoretical results which identified intercalated fullerides as suitable systems for hydrogen storage in mobile applications and its result meet many of the goals of the Swiss National Science Foundation *HyCarbo* project which constitutes the framework of the present research, addressed to the development of carbon-based materials for hydrogen storage applications.

As it was described in the previous sections, our efforts were devoted to the understanding of the mechanism of H_2 absorption and to the improvement of storage properties of these novel materials with the development of new strategies for the addition of transition metals to lithium intercalated fullerides. Some major results may be therefore summarized in:

- First observation of muon adduct radical within ionic systems, which we hope will stimulate some theoretical efforts devoted to understand its rather misterious formation.

- Understanding of fullerides hydrogenation mechanism: since this is a two step process composed by H_2 dissociation over intercalated clusters and H addition over charged fullerene, μSR allowed a separate study of atomic hydrogen chemisorption over C_{60}^{n-}, which was identified as a process independent from any temperature activation.

- H_2 molecule dissociation has been identified as the bottleneck that required improvement for an overall increase of lithium-fullerides performances, i.e through the addition of transition metal ions or particles.

- An innovative synthesis has been developed involving lithium-”*d*” block metal alloys for the addition of transition metal nanoparticles to Li intercalated fullerides and was applied to platinum and palladium.

- H_2 absorption properties (final uptake, kinetic properties) were clearly improved by Pt and Pd addition.

- The exploration of Pt, Pd stoichiometries suggested the transition metal subunit stoichiometry introduces a surface catalytic pathway in the H_2 dissociation maximizing materials’ properties.

- Too high TM stoichiometries resulted detrimental for absorption purposes as a result of the contemporary charge modification on C_{60}^{n-} and reduction of active, absorbing fraction.

- A solid state methathesis has been developed as suitable chemical reaction for the addition of other transition metals and rare-earths from their chloride salts (i.e Ni, Ti, Ce).

- Improvement of absorption properties is even met in case of nickel, titanium or cerium addition, surprisingly suggesting the observation of a H_2 dissociation promoted by both transition metals and rare earths.

- De-hydrogenation enthalpy suggests the addition of transition metal act as catalyst but not as a destabilizing agent towards hydrofullerene $C_{60}H_x$ since no significative changes can be detected in desorption phenomena of pure and doped samples.

- Reduction of transition metal particle size was identified as possible improvement in order to lower the de-hydrogenation enthalpy and it was gained with the development of a novel transition metal addition strategy based on metal-carbonyl clusters.

- Preliminary results seem to suggest the relativly sharp particle size distribution which are triggered by the use of metal clusters resulted in the contemporary improvement of H_2 absorption and destabilization of desorption process.

This work demonstrated and confirmed that both pure and hybrid alkali and transition metal intercalated fullerides are promising systems with respect to hydrogen as a fuel in mobile application. A more immediate summary of our results is pictured in Table 5.1. It is worth remembering here that US-DoE 2015 targets are 5.5 wt.% and an upper limit of 50 kJ/mol for the absorption amount and enthalpy, respectively.

	Abs. (wt.%)	Kinetic (wt.%/min)	De-H_2 Enthalpy (kJ/mol)
Li_6C_{60}	5	$4.3\cdot10^{-2}$	63
$Li_6Pt_{0.1}C_{60}$	5.9	$5.55\cdot10^{-2}$	62.9
$Li_6Pd_{0.07}C_{60}$	5.8	$6.77\cdot10^{-2}$	66
$Li_6Ni_{0.1}C_{60}$ ($NiCl_2$)	5.5	$5.27\cdot10^{-2}$	62.4
$Li_6Ni_{0.1}C_{60}$ (Clusters)	5.5	$5.46\cdot10^{-2}$	57.3

Table 5.1: Summary of hydrogen absorption properties in pure and transition metal doped lithium intercalated fullerides. Green color highlights improvement with respect to the pure material.

Unfortunately some properties of intercalated fullerides are still detrimental to their application in the field of hydrogen storage. The high temperatures needed to release H from fulleride systems, for instance, suggest harsh operative condition. Despite the improvements still needed, the relatively high absorption values discovered in both intercalated and hybrid fullerides identifies these systems as very promising.

Within this framework further developments can be easily imagined: 1- chemistry procedures can be further improved in order to exploit the clean, solid state synthesis to possibly control and even engineering hybrid carbon nanomaterials, 2- the control over size of transition metal particles and their reduction up to single atom decoration or intercalation moves towards hydrofullerene destabilization during desorption process or 3- different alkali intercalated fullerides may be imagined to overcome lithium too high stability. This production is therefore only the beginning of a completely new, fascinating and challenging research field, we strongly believe the best is yet to come!

Acknowledgements

First and foremost i would like to thank my supervisor, prof. Mauro Riccó, who decided to give me such a unique opportunity, for sharing science and knowledge, for his support, regard and friendship. It is my duty and pleasure to express gratitude to the skilled scientists i had the honour to work with, in particular i thank Daniele Pontiroli, Marcello Mazzani, Chiara Milanese, Samuele Sanna, Stephane Róls, Pawel Wzietek, Henri Alloul, Stephen Cottrell, Giovanni Bertoni, Pietro Galinetto and Sonia Pin for their teaching, collaboration, help and friendship. I officially ackowledge the ISIS - Rutherford Appleton Laboratory for beamtime provision. Many thanks to the people who have been my companions during this long trip...

References

[1] L. Schlapbach and A. Züttel, Hydrogen-storage materials for mobile applications, *Nature,*, vol. 414, 353 (2001). 1, 5

[2] J. van Vucht et al., *Philips Res. Rep.*, vol. 25, 133 (1970). 2

[3] U. Demirci et al., Ten years efforts and a no-go reccomendation for na borohydride for on-board automotive hydrogen storage, *Int. J. Hydrogen Energy*, vol. 34, no. 6, 2638 (2009). 2

[4] H. Kroto et al., C_{60}: buckminsterfullerene, *Nature*, vol. 318, 162 (1985). 2

[5] W. Kratschmer et al., Solid c_{60}: a new form of carbon, *Nature*, vol. 347, 354 (1990). 2

[6] P. Heiney et al., Orientational ordering transition in solid c_{60}, *Phys. Rev. Lett.*, vol. 66, 2911 (1991). 2

[7] D. Cox, Charachterization of c_{60} and c_{70} clusters, *J. Am. Chem. Soc.*, vol. 113, 2940 (1991). 3

[8] Q. Xie et al., Electrochemical detection of c_{60}^{+} and c_{70}^{+}: enhanced stability of fulleride solution, *J. Am. Chem. Soc.*, vol. 114, 3978 (1992). 3

[9] Y. Iwasa and T. Takenobu, Superconductivity, mott hubbard states and molecular orbital order in intercalated fullerides, *J. Phys. Cond. Matt.*, vol. 15, R495 (2003). 3

[10] P. Stephens et al., Structure of single phase superconducting k_3c_{60}, *Nature*, vol. 351, 632 (1991). 3

[11] R. Haddon, Conducting films of c_{60} and c_{70} by alkali metal doping, *Nature*, vol. 350, 320 (1991). 3

[12] O. Gunnarson, Superconductivity in fullerides, *Rev. Mod. Phys.*, vol. 69, 2 (1997). 4

[13] R. Kiefl et al., Evidence for endohedral muonium in k_xc_{60} and consequences for electronic structure, *Phys. Rev. Lett.*, vol. 69, no. 13, 2005 (1992). 4, 27

[14] C. Kuntscher and G. Bendele, Alkali metal stoichiometry and structure of k_4c_{60} and rb_4c_{60}, *Phys. Rev. B*, vol. 55, 3366 (1997). 4

[15] M. Rosseinsky, Recent developments in the chemistry and physics of metal fullerides, *Chem. Mater.*, vol. 10, 2665 (1998). 4

[16] S. Margadonna et al., Li_4c_{60}: A polymeric fulleride with a two-dimensional architecture and mixed interfullerene bonding motifs, *J. Am. Chem. Soc.* (2004). 4

[17] D. Quintavalle et al., Structure and properties of the stable two-dimensional conducting polymer mg_5c_{60}, *Phys. Rev. B*, vol. 77, 155431 (2008). 4

[18] T. Yildirim et al., Intercalation of sodium heteroclusters in the c_{60} lattice, *Nature,*, vol. 360, 568 (1992). 4, 10, 21, 32

[19] P. Stephens et al., Structure of rb:c_{60} compounds, *Phys. Rev. B*, vol. 45, 1 (1992). 4

[20] A. Ganin et al., Bulk superconductivity at 38 k in a molecular system, *Nature*, vol. 7, 367 (2008). 4

[21] N. Park et al., X-ray absorption near-edge structure (xanes) of iodine intercalated c_{60}: Evidence of ${i_2}^{\delta+}$ in $i_2c_{60}, Chem.\ Mater., vol.\ 8, 324 (1996). 4$

[22] K. Ishii et al., Ferromagnetism and giant magnetoresistance in the rare-earth fullerides $eu_{6-x}sr_xc_{60}$, *Phys. Rev. B*, vol. 65, 134431 (2002). 4

[23] S. Saito et al., Energetics and structural stability of cs_3c_{60}, *Solid State Comm.*, vol. 130, 335 (2004). 4

[24] H. Yoshikawa et al., Eu fulleride formation studied by photoemission spectroscopy, *Chem. Phys. Lett.*, vol. 239, 103 (1995). 4

[25] L. Chang and C. Hui-Ming, carbon nanotubes for clean energy applications, *J. Phys. D*, vol. 14, R231 (2005). 5

[26] H. Cheng et al., Molecular dynamics simulations on the effects of diameter and chirality on hydrogen adsorption on sw-nanotubes, *J. Phys. Chem. B*, vol. 109, no. 9, 3780 (2005). 5

[27] H. Tanaka et al., *J. Am. Chem. Soc.*, vol. 127, no. 20, 7511 (2005). 5

[28] H. Tanaka et al., *J. Phys. Chem. B*, vol. 108, no. 45, 17457 (2004). 5

[29] J. Sofo et al., Graphane: a two-dimensional hydrocarbon, *Phys. Rev. B*, vol. 75, 153401 (2007). 5

[30] P. Chen et al., *Science*, vol. 285, no. 5424, 91 (1999). 5

[31] H. Cheng et al., *Carbon*, vol. 39, no. 10, 1447 (2001). 5

[32] R. Yang, *Carbon*, vol. 38, no. 4, 623 (2000). 5

[33] M. Yoon et al., Charged fullerenes as high-capacity hydrogen storage media, *Nano Lett.*, vol. 7, no. 9, 2578 (2007). 5, 31, 51

[34] R. Lochan and M. Head-Gordon, *Phys. Chem. Chem. Phys*, vol. 8, no. 12, 1357 (2006). 6

[35] K. Chandrakumar and S. K. Ghosh, *Nano Lett.*, vol. 8, no. 1, 13 (2007). 6

[36] G. Kubas, Metal-dihydrogen and σ-bond coordination: the consummate extension of the dewar-chatt-duncanson model for metal-olefin π bonding, *J. of Organ. Chem.*, vol. 635, no. 1-2, 37 (2001). 6

[37] T. Hoang and D. Antonelli, Exploiting the kubas interaction in the design of hydrogen storage materials, *Adv. Mater.*, vol. 21, no. 18, 1787 (2009). 6

[38] W. Zhou et al., *Phys. Rev. B*, vol. 76, no. 8, 085434 (2007). 6

[39] E. Durgun et al., *Phys. Rev. Lett.*, vol. 97, no. 22, 226102 (2006). 6

[40] M. Dewar, *Soc. Chim. Fr.*, vol. 18, no. C71 (1951). 7

[41] M. Dewar, *Soc. Chim. Fr.*, vol. 18, no. C79 (1951). 7

[42] J. Chatt and L. Duncanson, Olefin co-ordination compounds. part iii. infra-red spectra and structure: attempted preparation of acetylene complexes, *J. Chem. Soc.*, vol. 49, 2939 (1953). 7

[43] T. Yildirim et al., *Phys. Rev. B*, vol. 72, no. 15, 153403 (2005). 7, 22, 58

[44] Y. Zhao et al., *Phys. Rev. Lett*, vol. 94, no. 15, 155504 (2005). 7

[45] W. Shin et al., *App. Phys. Lett.*, vol. 88, no. 5, 053111 (2006). 7, 22

[46] Q. Sun et al., *J. Am. Chem. Soc.*, vol. 128, no. 30, 9741 (2006). 7

[47] M. Yoon et al., *Phys. Rev. Lett*, vol. 100, no. 20, 206806 (2008). 7

[48] W. Conner and J.L.Falconer, Spillover in heterogeneous catalysis, *Chem. Rev.*, vol. 95, 759 (1995). 8

[49] A. Robell et al., Surface diffusion of hydrogen on carbon, *J.Phys.Chem.*, vol. 68, 2748 (1964). 8

[50] S. Srinivas and P. Rao, Direct observation of hydrogen spillover on carbon supported platinum and its influence on the hydrogenation of benzene, *J.Catal.*, vol. 148, 470 (1994). 8

[51] A. Lueking and R. Yang, Hydrogen spillover to enhance hydrogen storage-study of the effect of carbon physicochemical properties, *Appl. Catalysis A*, vol. 265, 259 (2004). 8

[52] Y. Li and R. Yang, Hydrogen storage on platinum nanoparticles doped on superactivated carbon, *J. Phys. Chem. C*, vol. 111, 11086 (2007). 8, 33

[53] C. Contescu et al., Detection of hydrogen spillover in palladium-modified activated carbon fibers during hydrogen adsorption, *J. Phys. Chem. C*, vol. 113, 5886 (2009). 8

[54] M. Zielinski et al., Hydrogen storage in nickel catalysts supported on activated carbon, *Int. J. Hydrogen Energy*, vol. 32, 1024 (2007). 8

[55] Q. Sun et al., Clustering of ti on a c_{60} surface and its effects on hydrogen storage, *J. Am. Chem. Soc.*, vol. 127, no. 42, 14582 (2005). 9

[56] M. Tomaselli et al., Nmr evidence for sp^3 carbon in the low-temperature phase of li_xc_{60}, *Phys. Rev. B*, vol. 63, 113405 (2001). 9

[57] J. Teprovich et al., Synthesis and characterization of a lithium-doped fullerane (li_x-c_{60}-h_y) for reversible hydrogen storage, *Nano Lett.*, vol. 12, 582 (2012). 9, 10, 21, 22, 33, 42, 45, 46, 50, 51

[58] P. Mauron et al., Reversible hydrogen absorption in sodium intercalated fullerenes, *Int. J. of Hydrogen Energy*, vol. 37, no. 19, 14307 (2012). 9, 21, 22, 30, 33, 46

[59] P. Mauron et al., Hydrogen absorption in $li_{12}c_{60}$, *J. Phys Chem. C*, vol. 117, no. 44, 22598 (2013). 9

[60] M. Tomaselli et al., *J. Chem. Phys.*, vol. 115, 472 (2001). 10, 31, 32

[61] C. Milanese et al., Effect of c (graphite) doping on the h_2 sorption performance of the mgni storage system, *Int. J. Hydrogen Energy*, vol. 35, 1285 (2010). 11

[62] R. Narayanan and R. Laine, Synthesis and characterization of precursors for group ii metal aluminates, *Appl. Organomet. Chem.*, vol. 11, 919 (1997). 11

[63] M. Bielmann et al., Characterization of hydrogen storage materials by means of pressure concentration isotherms based on the mass flow method, *Rev. Sci. Instr.*, vol. 80, 083901 (2009). 11

[64] B. Bandyopadhway et al., Development of asievert's type gas doping apparatus, *Bull. Mater. Sci.*, vol. 9, no. 4, 305 (1987). 11

[65] A. Coats and J. Redfern, Thermogravimetric analysis: A review, *Analyst.*, vol. 88, 906 (1963). 12

[66] C. Duval, *Inorganic Thermogravimetric Analysis*, Elsevier Amsterdam (1962). 13

[67] G. Hohne et al., *Differential Scanning Calorimetry - 2nd Ed.*, Springer-Verlag Berlin Heidelberg (2003). 13

[68] E. Watson and M. O'neill, *U.S. Patent*, vol. 3, no. 263, 484 (1962). 13

[69] E. Pungor, *A Practical Guide to Instrumental Analysis*, Florida: Boca Raton (1995). 14

[70] P. Mauron et al., High-pressure and high-temperature differential scanning calorimeter for combined pct measurements of hydrides, *Rev. Sci. Instr.*, vol. 80, 095113 (2009). 14

[71] H. Fecht et al., Nanocrystalline metals prepared by high-energy ball milling, *Metall. Mater. Trans.*, vol. A21, no. 9, 2333 (1990). 14

[72] I. Arita et al., Synthesis and processing of hydroxyapatite ceramic tapes with controlled porosity, *J. Mater. Sci. - Mater. Med.*, vol. 6, no. 1, 19 (1995). 14

[73] A. Sorrentino et al., Potential perspectives of bio-nanocomposites for food packaging applications, *Trends Food Sci. Technol.*, vol. 18, no. 2, 84 (2007). 14

[74] C. Suryanarayana, Mechanical alloying and milling, *Prog. Mater. Sci.*, vol. 46, 1 (2001). 14

[75] L. Takacs and V. Spelack, Quantitative comparison of the efficiency of mechanochemical reactors, *J. Mater. Sci.*, vol. 39, 5487 (2004). 15

[76] L. Takacs and J. McHenry, Temperature of the milling balls in shaker and planetary mills, *J. Mater. Sci.*, vol. 41, 5246 (2006). 15

[77] G. Fan et al., Metastable phases formation induced by mechanical alloying, *J. Mater. Sci.*, vol. 30, no. 19, 4847 (1995). 15

[78] S. Blundell, Spin-polarized muons in condensed matter physics, *Contemporary Physics*, vol. 40, no. 3, 175 (1999). 15

[79] J. Street and E. Stevenson, New evidence for the existence of a particle of mass intermediate between the proton and electron, *Phys. Rev.*, vol. 52, no. 9, 1003 (1937). 15

[80] R. Garwin, Observations of the failure of conservation of parity and charge conjugation in meson decays: the magnetic moment of the free muon, *Phys Rev.*, vol. 105, no. 4 (1415). 15

[81] D. Walker, Muon and muonium chemistry, cambridge university press (1983). 15

[82] S. Cox, Muonium as a model for interstitial hydrogen in the semiconducting and semimetallic elements, *Rep. Prog. Phys.*, vol. 72, 116501 (2009). 15

[83] A. Seeger, Positive muons and light isotopes of hydrogen, topics in applied physics, springer berlin-heidelberg, vol. 28, 349 (1978). 15

[84] S. Lee et al., Muon science, sussp, vol. 51 (1998). 16

[85] M. Luke et al., *J. Mag. Mag. Matrs*, vol. 754, 177 (1998). 17

[86] P. Réotier and A. Yaouanc, Muon spin rotation and relaxation in magnetic materials, *J. Phys. Cond. Matt.*, vol. 9, 9113 (1997). 17

[87] B. Webster and S. Kilcoyne, Muonium radical formation in apoferritin and ferritin, *Phys. Chem. Chem. Phys.*, vol. 1, no. 20, 4805 (1989). 18

[88] T. Yamazaki, Muon spin relaxation in magnetic materials, *Hyperfine Interactions*, vol. 6, no. 1-4, 115 (1979). 18

[89] R. Walstedt and L. Walker, Nuclear-resonance line shapes due to magnetic impurities in metals, *Phys. Rev. B*, vol. 9, no. 11, 4857 (1974). 18

[90] R. Kubo and T. Toyabe, Magnetic resonance and relaxation, ed r blinc amsterdam: North-holland, p. 810 (1967). 19

[91] R. Kubo, A stochastic theory of spin relaxation, *Hyperfine Interaction*, vol. 8, 731 (1981). 19

[92] A. Schenck, *Muon Spin Rotation Spectroscopy, Bristol Hilger* (1985). 19, 28, 29

[93] R. Hayano, Zero-and low-field spin relaxation studied by positive muons, *Phys. Rev. B*, vol. 20, no. 3, 850 (1979). 19

[94] A. Abragam, *Principles of Nuclear Magnetism, Oxford University Press* (1961). 19

[95] C. Slichter, *Principles of Magnetic Resonance, Springer series in Solid State Sciences* (1987). 19

[96] E. Roduner, The positive muon as a probe in radical chemistry, *Lecture Notes in Chemistry*, vol. 49 (1988). 19, 29

[97] S. Cox, Implanted muon studies in condensed matter science, *J. Phys. C: Solid State Phys*, vol. 20, 3187 (1987). 19

[98] S. Cox, Muon spin relaxation studies of interstitial and molecular motion, *Solid State Nuclear Magnetic Resonance*, vol. 11, 103 (1998). 19

[99] W. Moffatt, *The Handbook of Binary Phase Diagrams*, no. v. 4 in The Handbook of Binary Phase Diagrams, Genium Publishing Corporation (1987). 22

[100] T. Massalski, *Binary alloy phase diagrams*, v. 1-2, American Society for Metals Intl. (1990). 22

[101] M. Pozzo and D. Alfé, Hydrogen dissociation and diffusion on transition metal ([ti, zr, v, fe, ru, co, rh, ni, pd, cu, ag)-doped mg(0001) surfaces, *Int. J. of Hydrogen Energy,*, vol. 34, 1922 (2009). 22, 33, 61

[102] G. Longoni et al., Carbonylnickelates 1. synthesis and chemical characterization of the [ni5(c0)12]2- and [ni6(co)12]2-dianions, *Inorg. Chem*, vol. 15, 3025 (1976). 23, 62

[103] J. Calabrese et al., Synthesis and structure of a hexanuclear nickel carbonyl dianion,$[\mathrm{ni}_3(\mathrm{co})_3(2\text{-co})_3]_2^2$, and comparison with the $[\mathrm{pt}_3(\mathrm{co})_3(2\text{-co})_3]_2^2$ dianion. an unprecedented case of a metal cluster system possessing different metal architectures for congener transition metals, *J. Am. Chem. Soc.*, vol. 96, 2616 (1974). 23

[104] E. Ansaldo et al., Muonium in fullerite, *Nature,*, vol. 353, 121 (1991). 27

[105] E. Ansaldo et al., Formation of muonium and a muonic radical in fullerene, *Zeitschrift für Physik B Condensed Matter,*, vol. 86, no. 3, 317 (1992). 27

[106] C. Niedermayer, Fullerenes with μsr, *Hyperfine Interactions,*, vol. 97-98, no. 1, 285 (1996). 27

[107] W. MacFarlane et al., Muon-spin-relaxation studies of the alkali-fulleride superconductors, *Phys. Rev. B,*, vol. 58, no. 2, 1004 (1998). 27, 32

[108] F. Pratt, Repolarization of anisotropic muonium in orientationally disordered solids, *Phil. Mag. Lett.*, vol. 75, no. 6, 371 (1997). 29

[109] S. Cottrell et al., Muon charge state and dynamics in the alkali metal hydrides, *Physica B,*, vol. 289, 570 (2000). 31

[110] M. Capone et al., Theory of the metal-nonmagnetic mott-jahn-teller insulator transition in a_4c_{60}, *Phys. Rev. B*, vol. 62, 7619 (2000). 31

[111] Y. Lin et al., Hydrogen storage by spillover on graphene as a phase nucleation process, *Phys. Rev. B,*, vol. 78, 041402 (2008). 31

[112] B. I. Dunlap et al., Symmetric isomers of $c_{60}h_{36}$, *J. Phys. Chem.*, vol. 98, 1756 (1994). 31

[113] M. Kosaka et al., Superconductivity in $li_x csc_{60}$ fullerides, *Phys. Rev. B,*, vol. 59, R6628 (1999). 31

[114] R. F. Kiefl et al., Molecular dynamics of the muonium-c_{60} radical in solid c_{60}, *Phys. Rev. Lett.*, vol. 68, 2708 (1992). 32

[115] A. S. Lobach et al., Reaction of d_2 with palladium fulleride $c_{60}pd_{4.9}$, *Russ. Chem. Bull.*, vol. 45, no. 2, 464 (1996). 33

[116] A. Molodets et al., Stability of crystalline structure and molecules of hydrofullerene $c_{60}h_{36}$ under high shock pressures, *Doklady Physics*, vol. 53, no. 11, 562 (2008). 34, 35, 62

[117] M. Ricco et al., Superionic conductivity in the li_4c_{60} fulleride polymer, *Phys. Rev. Lett.*, vol. 102, no. 14, 145901 (2009). 33

[118] O. Paschos et al., Synthesis of platinum nanoparticles by aerosol assisted deposition method, *Thin Solid Films*, vol. 516, no. 12, 3796 (2008). 35

[119] J. Langford and A. Wilson, Scherrer after sixty years: A survey and some new results in the determination of crystallite size., *J. Appl. Crystallography*, vol. 11, no. 2, 102 (1978). 35

[120] M. Riccó et al., Recovering metallicity in a_4c_{60}: The case of monomeric li_4c_{60}., *Phys. Rev. B*, vol. 75, no. 8, 081401 (2007). 35

[121] M. Aramini et al., Muon spin relaxation reveals the hydrogen storage mechanism in light alkali metal fullerides, *Carbon*, vol. 67, 92 (2014). 42

[122] H. Marand et al., Influence of structural and topological constraints on the crystallization and melting behavior of polymers. 2. poly(arylene ether ether ketone), *Macromolecules*, vol. 33, 3392 (2000). 45, 61

[123] M. Aramini et al., Addition of transition metals to lithium intercalated fullerides enhances hydrogen storage properties, *Int. J. Hydrogen Energy*, vol. 39, no. 5, 2124 (2013). 45, 49

[124] M. Dornheim et al., Hydrogen storage in magnesium-based hydrides and hydride composites, *Scripta Mater.*, vol. 56, 841846 (2007). 46

[125] J. Yang et al., Destabilizing libh4 with a metal (m = mg, al, ti, v, cr, or sc) or metal hydride (mh2 = mgh2, tih2, or cah2), *J. Phys. Chem. C*, vol. 111, 19134 (2007). 46

[126] X. Zhang, Homolytic bond dissociation enthalpies of the c-h bonds adjacent to radical centers, *J. Org. Chem.*, vol. 63, 1872 (1998). 46

[127] A. Talyzin, Fulleranes by direct reaction with hydrogen gas at elevated conditions, *Carbon Mat.: Chem. and Phys.*, vol. 2, 85 (2010). 46

[128] A. Talyzin et al., Comparative study of hydrofullerides c60hx synthesized by direct and catalytic hydrogenation, *Appl. Phys. A*, vol. 78, 1005 (2004). 46

[129] T. Guo and G. Scuseria, Ab initio calculations of tetrahedral hydrogenated buckminsterfullerene, *Chem. Phys. Lett.*, vol. 101, no. 6, 527 (1992). 46

[130] T. Scheler et al., Synthesis and properties of platinum hydride, *Phys. Rev. B*, vol. 83, 214106 (2011). 46

[131] W. Bronger, Synthesis and structure of new metal hydrides, *J. Alloys and Compounds*, vol. 229, 1 (1995). 46

[132] W. Bronger and L. Brassard, $Li_5pt_2h_9$, a complex hydride containing isolated [pt2h9]5- ions, *Angew. Chem. Inr. Ed. EngI.*, vol. 34, no. 8, 898 (1995). 46

[133] A. Graefe and R. Robeson, Reactions of transition metals with lithium hydride-hydrogen at elevated temperatures, *J. lnors, nucl. Chem*, vol. 29, 2917 (1967). 46

[134] B. Nacken and W. Bronger, Uber die systeme liypthx und liypdhx, *J. Less-Common Metals*, vol. 52, 323 (1977). 46

[135] R. Baranova et al., Crystal structure of palladium hydride with primitive cubic lattice, *Kristallografiya*, vol. 25, 1290 (1980). 46

[136] S. Kennedy et al., Ordering of deuterium in $pdd_{0.65}$ at 54 k, *J. Phys.: Cond. Matt.*, vol. 7, L33 (1995). 46

[137] T. Skoskiewiz and B.Baranowski, *Phys. Status Solidi*, vol. 30, K33 (1968). 46

[138] T. Wagberg et al., Structural aspects of two-dimensional polymers: Li_4c_{60}, na_4c_{60} and tetragonal c_{60}. raman spectroscopy and x-ray diffraction., *J. Phys. Chem. Solids*, vol. 65, 317 (2004). 50

[139] F. Borondics et al., Polymeric sheets in mg_4c_{60}., *Solid. State Comm.*, vol. 127, 311 (2003). 50

[140] R. Haddon et al., Conducting films of c_{60} and c_{70} by alkali-metal doping, *Nature*, vol. 350, 320 (1991). 50

[141] T. Makarova et al., Experimental realization of high spin states in dilutely hydrogenated fullerenes., *Phys. Status Solidi*, vol. 246, no. 11-12, 2778 (2009). 50

[142] C. Jensen and K. Gross, Development of catalytically enhanced sodium aluminum hydride as a hydrogen-storage material, *Appl. Phys. A*, vol. 72, 213219 (2001). 56

[143] S. Foiles et al., Calculation of hydrogen dissociation pathways on nickel using the embedded atom method, *J. Less Comm. Metals*, vol. 130, 465 (1987). 56

[144] H. Adachi et al., Cluster calculation of the electronic structure of interstitial hydrogen in ti, ni and pd, *J. Phys. Soc. Jap.*, vol. 44, no. 3, 1039 (1978). 56

[145] T. Upton and W. Goddard, Chemisorption of atomic hydrogen on large nickel cluster surface, *Phys. Rev. Lett.*, vol. 42, no. 7, 472 (1979). 56

[146] A. Martensson et al., Adsorption of hydrogen on a stepped nickel surface, *Surface Science*, vol. 205, 12 (1988). 56

[147] A. Hamza and R. Madix, Dynamics of the dissociative adsorption of hydrogen on ni(100), *J. Phys. Chem.*, vol. 89, no. 25, 5381 (1985). 56

[148] S. Stopic et al., Effect of pd, cu, and ni additions on the kinetics of nicl$_2$ reduction by hydrogen, *Metallurgical and materials Trans. B*, vol. 28B, 1241 (1997). 60

[149] B. Epstein, The mathematical description of certain breakage mechanisms leading to the logarithmico-normal distribution, *J. Franklin Inst.*, vol. 244, no. 6, 471 (1947). 63

[150] Z. Cheng and S. Redner, Kinetics of fragmentation, *J. Phys. A: Math. Gen.*, vol. 23, 1233 (1990). 63